

Department of Electrical Engineering and Information Technology

Master Thesis
for attainment of the academic degree of
Master of Engineering (M. Eng.)

Measurement and Simulation of Mutual Coupling Effects between
Dual-Polarized L-Band Horn Antennas for Satellite-Based Radar System
Calibration

Presented by:	B. Eng. Anna Maria Büchner
Born on:	24.10.1994
Enrolment number:	637 132
Seminar group:	01 RFE
Academic supervisor:	Prof. Dr.-Ing. Ludwig Niebel
Mentor (DLR Institute HR):	Dr. rer. nat. Klaus Frank Weidenhaupt
Issue date:	22.05.2019
Handover date:	10.07.2019

Acknowledgement

First of all, I would like to thank my mentor Dr. rer. nat. Klaus Weidenhaupt from the Microwave and Radar Institute of DLR Oberpfaffenhofen for his support, the proof-reading of my thesis and laughs along the way.

I would also like to thank Dr.-Ing. Marco Schwerdt for making the time to provide valuable input and expertise for this thesis. I also want to thank him for making my continued participation in the REXUS/BEXUS program alongside my work possible.

Thank you also to Prof. Dr.-Ing. Ludwig Niebel for accompanying me as a professor through my bachelor and master studies as well as agreeing to be the academical supervisor of my master thesis.

For the construction of the mechanical setup, I would like to thank Peter Heitzer from the Institute's mechanical lab. A much needed thank you also goes to all colleagues for the welcome distractions during lunch breaks and for making me feel welcome from the start.

Last but not least, I would like to thank my family for their continuous support and pep talks. For his kind words and never ending encouragement I want to thank my boyfriend. Also, I'm grateful for my friends who, no matter how far away I moved, always supported me with advice and made me believe in myself.

Contents

List of Figures	V
List of Tables	VIII
List of Abbreviations	IX
List of Symbols	X
Abstract	XI
1 Context	13
1.1 Motivation	13
1.2 Synthetic Aperture Radar	14
1.3 SAR System Calibration	15
1.4 DLR's SAR Calibration Transponders	17
2 Antenna Theory	18
2.1 Radiation Patterns	18
2.1.1 Field Regions	20
2.2 Directivity and Gain	21
2.3 Polarization Loss Factor	22
2.4 Waveguides and Modes	24
2.5 Transmission Lines	25
2.6 S-Parameters	27
3 The VeGA Antenna	29
3.1 Antenna Flare	29
3.2 Orthomode Transducer	30
3.3 Hybrid Feed Network	30
3.4 Final Design	32
4 Simulation	35
4.1 Simulation Setup	36
4.2 Simulation Results	41
4.2.1 Single Antenna	41
4.2.2 Double Antenna Setup	44
5 Measurements	50
5.1 Mechanical Setup	50
5.2 Tuning of the Hybrid Feed Network	52
5.3 Measurement Setup	53

5.4	Measurement Results	54
5.4.1	Normal Antenna Setup	54
5.4.2	Absorbers	59
6	Conclusion and Outlook	62
	Bibliography	64
A	Appendix	68
A.1	Antenna Model	68
A.2	Hybrid Feed Networks	69
A.3	Absorber Measurements	71
A.4	German Translation of Important Terms	75
	Theses	76
	Statement of Authorship	77

List of Figures

1-1	Illustration of the SAR imaging principle (from [1] (p. 10))	14
1-2	Comparison between SAR images from the 1990s (a) and 2007 acquired with TerraSAR-X (b), showing a clearly improved resolution of the pyramids of Giza, Egypt (from [1](p. 8))	15
1-3	Block diagram of a Kalibri transponder (from [2])	17
1-4	Kalibri C-band transponder without the 2-axis positioner (from [3]) . .	17
2-1	Simplified visualization of an antenna and additional components necessary to transmit radio waves	18
2-2	Three-dimensional spherical coordinate system	19
2-3	Radiation pattern of the VeGA antenna	19
2-4	Propagation of the electrical field vector over time (left) and trace of the vector projected on a reference plane (right) (from [4](p. 67))	19
2-5	Co- and cross-polarization pattern of the choked Gaussian horn antenna (German: Verkürzte Gauß-Hornantenne) (VeGA) antenna	20
2-6	Calculated polarization loss factor over ψ	23
2-7	Depiction of the wave propagation in waveguides (top view) with $m = 1, 2, 3, \dots$ (adapted from [5])	24
2-8	Depiction of the field lines within a rectangular waveguide where the drawn through lines represent the electric field and the dashed lines the magnetic field. (adapted from [6](p. 332))	25
2-9	Equivalent circuit diagram of a small section of a coaxial line (adapted from [7](p. 157))	26
2-10	Depiction of the s-parameters of a 2-port network with the incident and reflected waves	28
3-1	Antenna flare of the VeGA antenna [8](p. 39)	29
3-2	Layout of a planar OMT (adapted from [9])	30
3-3	Geometry of the optimised OMT including waveguide step and tuning stub (from [10](p. 44))	30
3-4	Diagram of the hybrid feed network (top, adapted from [11, p. 10]) and picture of a hybrid feed network used for measurements (bottom) . . .	31
3-5	Structure of a 180° ring coupler in microstrip line or stripline form (left) and its ideal scattering matrix (right, from [12](p.363))	31
3-6	All three versions of the VeGA antenna. On top and mounted on the compact test range (CTR) positioner is the aluminium antenna, left is the carbon fiber reinforced polymer (German: Carbonfaserverstärkter Kunststoff) (CFK) antenna and on the right is the 3D-printed antenna. (from [11](p. 7))	32

3-7	Co-polarization (left) and cross-polarization (right) of the aluminium, CFK and the 3D-printed VeGA antenna (from top to bottom, taken from [11](p. 15)	33
4-1	Antenna model setup	36
4-2	Illustration of horizontal and vertical polarizations for both antennas including the numbers of the hybrid feed networks	37
4-3	Relation between polarization sets and s-parameters	37
4-4	Connection of hybrid coupler 1 to antenna 1	38
4-5	Visualization of different distances between the antennas	39
4-6	Reflections for a single antenna in comparison to the reflection of the CTR measurement as a function of the frequency	41
4-7	Inter-channel-coupling for a single antenna in comparison to the CTR results as a function of the frequency	42
4-8	Gain pattern at $\phi = 0^\circ$ in co- and cross-polarization of the simulation and measurement	43
4-9	Gain pattern at $\phi = 45^\circ$ in co- and cross-polarization of the simulation and measurement	44
4-10	Co- and cross-coupling for f_0 over d_sweep	45
4-11	Co- and cross-coupling for f_0 over α_sweep	46
4-12	Comparison of different co-polarization gain patterns	47
4-13	Comparison of different cross-polarization gain patterns	48
4-14	Near field at $z = 500\text{mm}$ for the single antenna and double antenna setup with a distance of $d_sweep = 1\text{ m}$ and $d_sweep = 2.25\text{ m}$ with the color scale representing the electric field strength.. (see text for details)	49
5-1	Antenna fixture during the assembly for the outside measurement (left: stationary aluminium antenna, right: movable CFK antenna	50
5-2	Close up image of the measurement setup (visible: hybrid feed networks, laser range finder as well as indicators for the rotation)	51
5-3	Measurement setup for the tuning of the hybrid couplers	52
5-4	Magnitude and phase characteristic of feed network 1 for $f_0 \pm 250\text{MHz}$	53
5-5	Schematic drawing of the measurement setup showing both antennas as well as all feed networks and the vector network analyser (VNA)	54
5-6	Co-coupling for f_0 over d_sweep	55
5-7	Co-coupling coefficient S_{31} over $f_0 \pm 58\text{ MHz}$	56
5-8	Cross-coupling coefficient S_{32} over $f_0 \pm 58\text{ MHz}$	57
5-9	Inter-channel-coupling for f_0 over d_sweep	57
5-10	Reflections for f_0 over d_sweep	58
5-11	Co- and cross-coupling for f_0 over α_sweep	59

5-12	Picture of setup 4.3 with an illustration of the corresponding top view, where the absorber placement is marked by red crosses	60
5-13	Co-coupling coefficient S_{31} over $f_0 \pm 52.5$ MHz of setup 4	60
A.1-1	Networks of the model in the schematic view for the calculation of the field patterns with horizontal polarisation of the first antenna. Not visible in this view are the voltage sources connected to the terminals HC1.4	68
A.1-2	Representation of the requested fields for the antenna model	68
A.2-3	Magnitude and phase characteristics of all hybrid feed networks	70
A.3-4	Setup 1	71
A.3-5	Co-coupling coefficient S_{31} over $f_0 \pm 52.5$ MHz of setup 1	71
A.3-6	Setup 2.3	72
A.3-7	Co-coupling coefficient S_{31} over $f_0 \pm 52.5$ MHz of setup 2	72
A.3-8	Setup 3.3	73
A.3-9	Co-coupling coefficient S_{31} over $f_0 \pm 52.5$ MHz of setup 3	73
A.3-10	Setup 5	74
A.3-11	Co-coupling coefficient S_{31} over $f_0 \pm 52.5$ MHz of setup 5	74

List of Tables

4-1	Port mapping between hybrid couplers and antennas	38
4-2	Values for both sweep parameters	40

List of Abbreviations

API	application programming interface
CEM	computational electromagnetic
CFK	carbon fiber reinforced polymer (German: Carbonfaserverstärkter Kunststoff)
CTR	compact test range
DLR	German Aerospace Center (German: Deutsches Zentrum für Luft- und Raumfahrt)
ESA	European Space Agency
GPHA	gaussian profiled horn antenna
GPS	global positioning system
GUI	graphical user interface
MOM	method of moments
OMT	orthomode transducer
PCB	printed circuit board
RCS	radar cross section
Rx	receiver
SAR	synthetic aperture radar
SLAR	side looking aperture radar
TE	transverse electric
TM	transverse magnetic
Tx	transmitter
VeGA	choked Gaussian horn antenna (German: Verkürzte Gauß-Hornantenne)
VNA	vector network analyser

List of Symbols

c	Speed of light
C'	Capacitance between both conductor lines
D_A	Largest dimension of the antenna
$D(\theta, \phi)$	Directivity in a given direction
f	Frequency
G	Gain
G'	Isolation between the conducting wires
L'	Inductance of the transmission line
P_{in}	Input power
P_{loss}	Power dissipation
PLF	Polarization loss factor
P_{rad}	Radiated power
r	Distance from the antenna
R_1	Boundary between reactive and radiating near field
R_2	Boundary between radiating near field and far field
R'	Resistance of the transmission line
S_i	Power density of an isotropic antenna
S_{ij}	S-parameter
S_{max}	Maximum power density
$S(\theta, \phi)$	Power density in a given direction
\underline{Z}_0	Wave impedance
\underline{Z}_L	Transmission line impedance
$\underline{\Gamma}$	complex reflection coefficient
η_0	Total efficiency
η_A	Radiated antenna efficiency
η_c	Conduction efficiency
η_d	Dielectric efficiency
λ	Wavelength
ρ_w	Unity vector of the electrical field of the incoming wave
ρ_a	Unity vector of the electrical field of the receiving wave
ψ	Angular deviation between incoming and receiving polarization

Abstract

To calibrate spaceborne synthetic aperture radar (SAR) systems for global Earth observation, active and passive reference targets are used. Transponders are active reference targets with a high radar cross section (RCS) at a compact design and have been developed at the Microwave and Radar Institute of German Aerospace Center (German: Deutsches Zentrum für Luft- und Raumfahrt) (DLR) for more than 20 years. For upcoming missions in L-band the Institute is developing a new generation of their accurate so-called Kalibri transponders.

These transponders are based on a two antenna design: one antenna to receive electromagnetic pulses from the SAR system and another to retransmit the amplified pulse to the SAR system. After processing the radar data, the transponder becomes clearly visible in the scattering image recorded by the SAR system as a bright signature with calibrated signal strength.

In order to achieve stable transponders with an accurate RCS for the demanding calibration tasks of the SAR system, the decoupling between both antennas should be as high as possible. The requirement derived from the specifications of the SAR system and the electrical design of the calibration transponder demands a decoupling better than 90 dB. As the dual-polarized L-band horn antenna to be used in the "Kalibri - Next Generation" transponders has been newly developed by German Aerospace Center (German: Deutsches Zentrum für Luft- und Raumfahrt) (DLR), the mutual coupling between two antennas of this type has yet to be quantified and investigated.

First, the key theoretical principles are introduced. Subsequently, the structure of the developed antenna as well as its two channel feeding system is described.

Furthermore, a simulation setup is developed in the course of this thesis, which represents the physical antenna with its feeding system. This model is verified by comparing it to previously made CTR measurements. To conduct simulations for the mutual coupling with regard to the distance between the antennas the simulation model is adapted to include a second antenna. In addition, the effect of a polarization misalignment on the antenna coupling is simulated.

A measurement setup is designed and built to perform the same parameter variations as was done for the simulations. Therefore the mechanical setup enables the positioning of two antennas on a rail structure. This allows for a variation of the distance between the antennas. Additionally, a rotation of one antenna is possible. With this setup, the needed distance to fulfil the decoupling requirement can be determined. In addition

to the distance variation and change of polarization misalignment, experiments with absorbers are conducted to further lower the mutual antenna coupling.

The results of this thesis are vital for the design of DLR's "Kalibri - Next Generation" transponders as the distance between the antennas has a major influence and impact on the overall transponder design.

1 Context

1.1 Motivation

The Microwave and Radar Institute of DLR has contributed to various successful spaceborne SAR missions deployed for global Earth observation, such as TerraSAR-X (DLR) and TanDEM-X (DLR) as well as Sentinel-1 (ESA) and is specialized in SAR techniques and systems. [13]

With the years, the Institute has deployed and established the DLR SAR Calibration Center for the calibration of spaceborne SAR systems. For the calibration of future missions in the L-band (1 GHz to 2 GHz) such as TanDEM-L (DLR) and ROSL (European Space Agency (ESA)) a new generation of reference targets is currently in development. For these so-called "Kalibri - Next Generation" transponders a new horn antenna was designed. This so-called choked Gaussian horn antenna (German: Verkürzte Gauß-Hornantenne) (VeGA) antenna is based on a two channel concept to be able to receive and transmit a horizontal as well as a vertical polarization simultaneously. It is referred to as dual-polarized VeGA antenna. [2] Each transponder employs two antennas, one for receiving the signal and one for transmitting the amplified signal back to the SAR system. The transponder is used as a reference for the accurate calibration of the SAR system. To perform a successful calibration the reference target has to be highly accurate as well and stable in its performance. [3] The mutual coupling of the antennas in the transponder strongly influences these characteristics, which is why the coupling is required to be extremely low.

The predecessors of the "Kalibri - Next Generation" transponders normally operate with an orthogonal alignment of the received and transmitted polarization [14] in order to achieve a decoupling of at least 90 dB. With the new VeGA antenna design both polarisations are excited simultaneously. This means an orthogonal offset is no longer possible. As a consequence the coupling of the antennas has to be reduced by other means.

This thesis sets out to investigate and quantify the mutual coupling of the new VeGA antennas by conducting simulations and measurements. The dependency of the coupling on the distance between the antennas as well as the effect of angular polarization misalignment is assessed.

The goal of this thesis is to provide a recommendation regarding the integration of the L-band VeGA antennas in DLR's next generation of transponders. The results are decisive for the development of the new transponder design.

1.2 Synthetic Aperture Radar

Synthetic aperture radar (SAR) is a technology to gather high-resolution radar images of the Earth without limitations due to weather or the day-and-night cycle. SAR systems are based on side looking aperture radar (SLAR). To improve the image resolution without increasing the physical antenna length of the antenna, the aperture of the radar antenna is synthetically enlarged by recording a scene with more than one radar pulse during an overpass. As mentioned in [1](p. 7), this was made possible by an invention of Carl Wiley in 1951, which was improved upon and lead to the final principle as it is, in particular, used like today for global Earth monitoring from space.

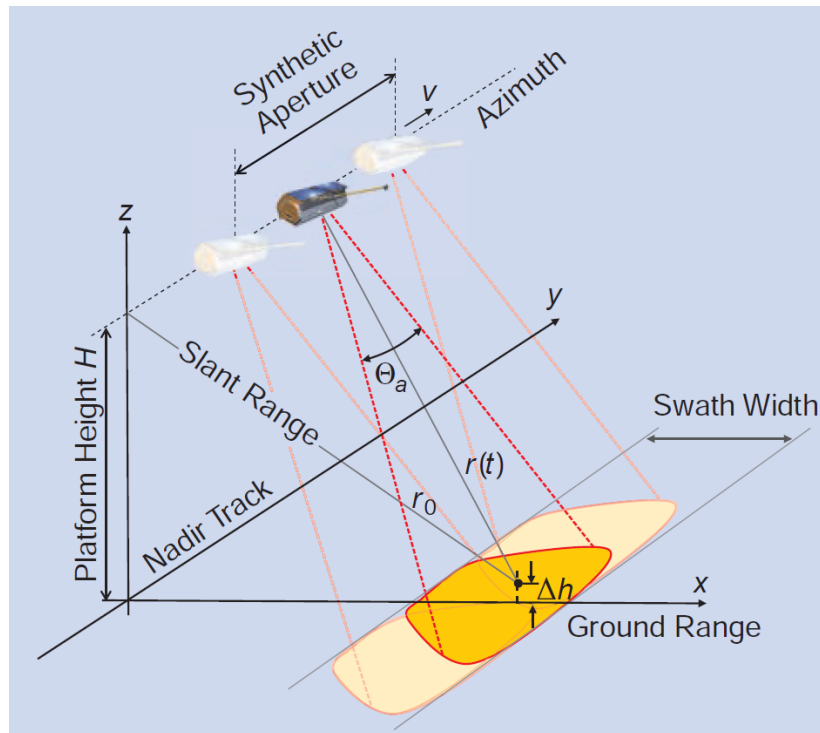


Figure 1-1: Illustration of the SAR imaging principle (from [1] (p. 10))

Figure 1-1 shows the principle of SAR imaging. The transmitted radar pulse illuminates a portion of the ground, which turns into a strip due to the movement of the satellite along azimuth. A SAR system records the backscattered signal of the ground as it is passing over it. The received radar pulses are combined into a coherent SAR image. This combination results in a synthetic enlargement of the aperture of the antenna, which is longer than the actual physical antenna length. [1](p. 8-9)

An actual representation of the acquired scene is only achieved after processing the recorded raw data. An example for SAR images is given in figure 1-2. Depicted is the same geographical location recorded in the 1990s with a resolution of 20 m in C-band (a) and 2007 with a resolution of 1 m in X-band with TerraSAR-X (b).

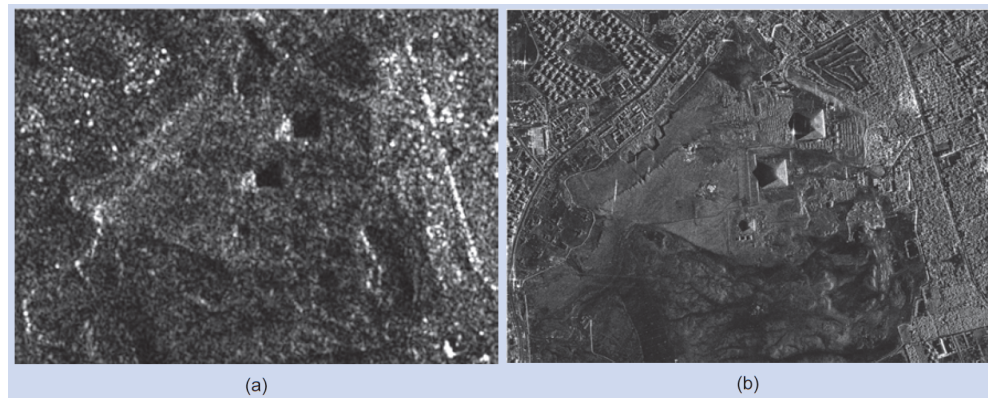


Figure 1-2: Comparison between SAR images from the 1990s (a) and 2007 acquired with TerraSAR-X (b), showing a clearly improved resolution of the pyramids of Giza, Egypt (from [1](p. 8))

SAR technology can be used for various applications in Earth observation. Some examples are:

1. monitoring of disasters like earthquakes, floodings, landslides or oil catastrophes,
2. mapping of glacial movement,
3. traffic monitoring,
4. tracking of deforestation and
5. recording of a global digital elevation model as done by TanDEM-X.

An in-depth overview on the various SAR techniques needed to provide the data for said examples is given in [1].

A single SAR provides two-dimensional pictures, but as demonstrated by the TanDEM-X mission, a precise digital elevation model of the earth's surface can be generated by using two satellites equipped with SAR systems flying in close formation. [1](p. 20-23)

1.3 SAR System Calibration

The image data acquired with the SAR system has to be calibrated before the image information can be transformed into geophysical units. The calibration of a SAR system is understood to include all procedures required to eliminate errors. This includes system instabilities like thermal drift or offsets. It is differentiated between internal calibration through online monitoring of the instrument with calibration pulses within the SAR instrument and external calibration through the measurement of the SAR system against reference targets on Earth.[15](p. 15)

For external calibration of a SAR system various reference targets are placed on the ground. These targets are distinguished in passive and active targets. An example for passive reference targets are corner reflectors, while active targets are so-called transponders. Corner reflections can be used for geometric and radiometric calibration, while so-called ground receivers or the Amazon rain forest are utilized for antenna pattern verification and pointing determination. (More information can be found in [15](p. 18-19).) Transponders have proven to be advantageous for various other calibration tasks and have a high RCS at a compact design in comparison to corner reflectors.

The essential characteristics of transponders are the high RCS at compact design and the adjustability of their RCS through electrical amplification without the need of increasing their physical size. This separates them from corner reflectors as structural limitations have an impact on their maximum reachable RCS and their RCS can not be adjusted after they have been produced.

Due to their high RCS, transponders are used for absolute radiometric calibration. This calibration is needed to transform the image information into geophysical units and thus to derive the backscattering characteristics of the different objects within the SAR scene. [15](p. 18) The transponder will appear as a bright signature in the SAR image.

In addition to this, transponders can be employed for polarimetric calibration. During polarimetric calibration a 2×2 scattering matrix is recorded by the SAR system. This matrix represents all four relations of the received to the transmitted polarizations of the SAR system. With a transponder both horizontal and vertical polarizations can be received and retransmitted simultaneously. Depending on the settings, the signal can also be re-transmitted only with the same or contrasting polarization as received by the transponder. This way all possible s-parameter combinations and thus a reference target with a complex scattering matrix can be provided during an overpass. This is important for polarimetric calibration in order to determine the channel imbalance and the cross talk of a full polarimetric SAR system. [1](p. 14)

As it is possible to record the received signal, the transponder can also be used to verify the transmitting antenna patterns and the pointing of a SAR system. [15](p. 18)

1.4 DLR's SAR Calibration Transponders

Reference targets such as transponders for the external calibration of SAR systems have been developed and used by the Microwave and Radar Institute of DLR for more than 20 years. [13]

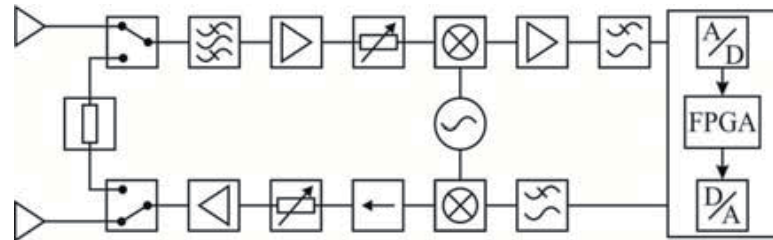


Figure 1-3: Block diagram of a Kalibri transponder (from [2])

The so-called Kalibri transponder has been developed for X- and C-band and is based on a two antenna design. Figure 1-3 shows the block diagram of the transponder. The signal transmitted by the SAR system is received by the first antenna and fed into the receiver chain. After filtering and adjusting the signal to the correct levels, the signal is converted from analog to digital. The FPGA is then used to process and store the sampled signals. After this and a conversion from digital to analog, the signal is amplified and adjusted to the desired RCS value in the transmitter chain. A more detailed description of the block diagram can be found in [2]. The very stable RCS over the lifetime of the transponder is guaranteed by an internal calibration loop. [2](p. 3) To compensate for temperature effects of the electronics, the components are accommodated in a temperature stabilized housing. The antenna apertures are covered by radomes made out of Teflon. [2](p. 2) The transponder has a radiometric stability of approximately 0.1 dB and a RCS of about 60 dB m² at C-band (5.4 GHz). [2](p. 1)

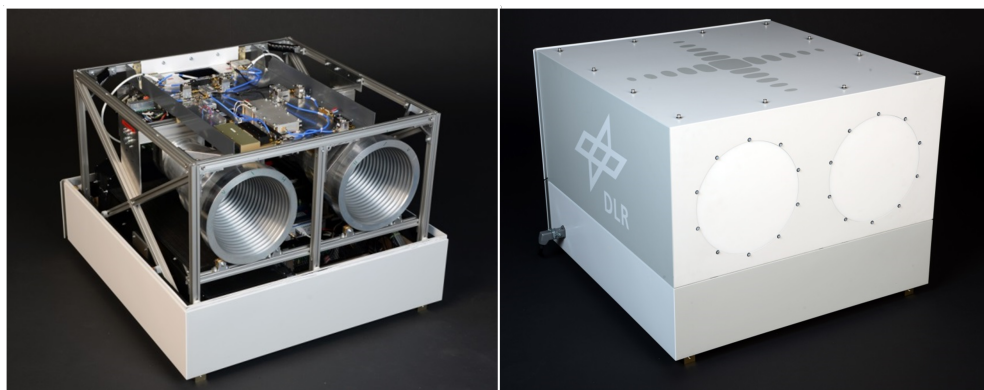


Figure 1-4: Kalibri C-band transponder without the 2-axis positioner (from [3])

Figure 1-4 shows the Kalibri C-band transponder with its corrugated horn antennas. During the overpass of the satellite the transponder has to be aligned in azimuth and elevation. To make the necessary precise alignment possible, the transponder is placed on a 2-axis positioner. [3]

2 Antenna Theory

A structure that enables the transition of a guided wave into free-space and vice versa can be classified as an antenna. [16] (p. 12) As a result, the antenna is referred to either as a transmitting or a receiving antenna.

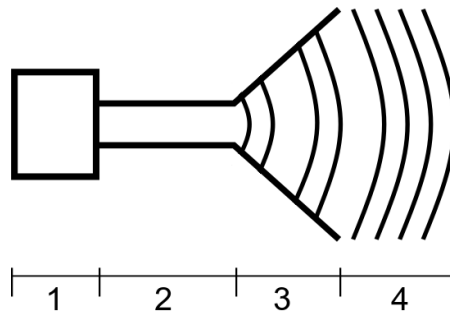


Figure 2-1: Simplified visualization of an antenna and additional components necessary to transmit radio waves

A device to realize this transition is made up of an antenna, which is connected to a guiding device and a source or receiver. Figure 2-1 shows the overall structure of such a device for the transmitting case. The numbered elements are called source (1), transmission line (2), antenna (3) and radiated free-space wave (4). To receive radio waves the source is exchanged for a receiver, while all other parts remain the same.

The reciprocity theorem can be applied to antennas. Therefore, the antenna properties for the transmit and receive case are identical. Consequently, the antenna characteristics are identical in both cases as well. [4] (p. 140-143)

2.1 Radiation Patterns

The radiation pattern represents the radiation properties of an antenna depending on the space coordinates. The measured pattern is identical in both transmit and receive mode, due to reciprocity.

With the angles ϕ and θ of a spherical coordinate system as shown in figure 2-2 every point of the three-dimensional pattern can be addressed. ϕ is also known as azimuth angle and θ is known as elevation angle. For the comparison of antenna performance, two-dimensional patterns are convenient. These plots represent a cut through the three-dimensional pattern of the antenna. The pattern can also be plotted in a polar coordinate system.

In this thesis all patterns are plotted as power patterns in dB. Figure 2-3 shows the three-dimensional pattern of the VeGA antenna. The definable sections of the antenna

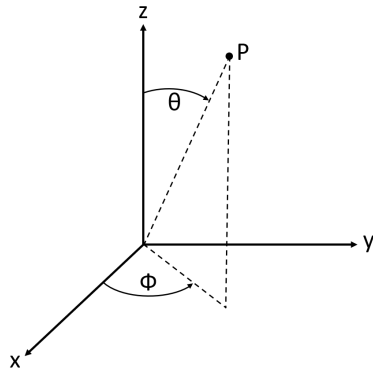


Figure 2-2: Three-dimensional spherical coordinate system

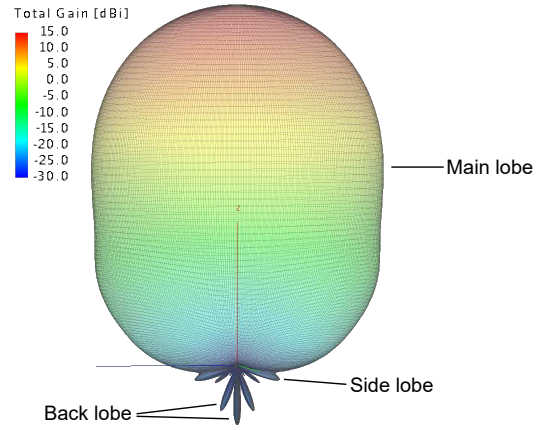


Figure 2-3: Radiation pattern of the VeGA antenna

pattern are called lobes. Between them are sections of relatively low radiation intensity. The lobe with the maximal radiated power is the main lobe. In this pattern the maximum of the main lobe is located at $\phi = 0$ and $\theta = 0$. Lobes in the opposite direction from the main lobe are known as back lobes while every lobe in between is called side lobe. [4](p. 26-28)

In the far field (see chapter 2.1.1), the electric and magnetic field of a propagating wave are perpendicular to each other as well as perpendicular to the propagation direction. To determine the polarization of this propagating wave, the instantaneous electric field vector is observed over time. [4](p. 66)

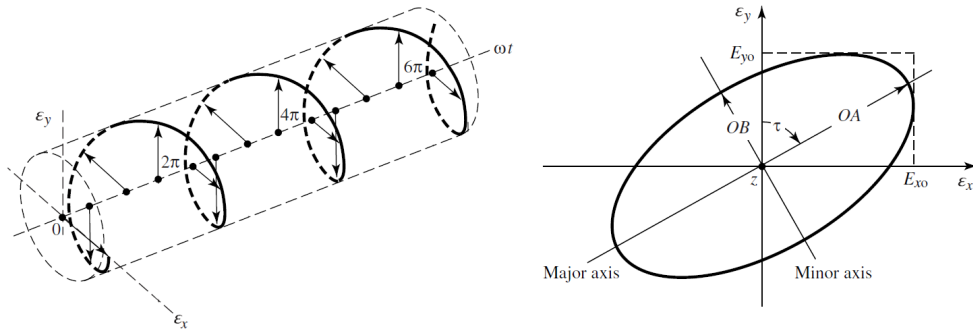


Figure 2-4: Propagation of the electrical field vector over time (left) and trace of the vector projected on a reference plane (right) (from [4](p. 67))

Figure 2-4 shows the propagation of the electric field vector with components in x and y direction as a function of time. If the curve traced by the end point of the vector is projected onto a reference plane (as depicted on the right), it shows the polarization of the electric field of the propagation wave. Generally, the traced figure is an ellipse where the polarization is elliptic and might be tilted with an angle of τ . Special cases like $OA = OB$ and $OA = 0$ or $OB = 0$ are known as circular and linear polarizations. The antennas in this thesis are linear polarized. [4](p. 66-67)

One possibility to present the radiation pattern of an antenna is based on the third definition of Arthur C. Ludwig from 1973. There, the radiation pattern is split into two depictions, which are referred to as co- and cross-polarization. [17] In general, the co-polarization describes the radiation of the antenna in its intended polarization. Therefore, the cross-polarization depicts the parasitic and usually unwanted radiation of the antenna in the opposite of the intended polarization.

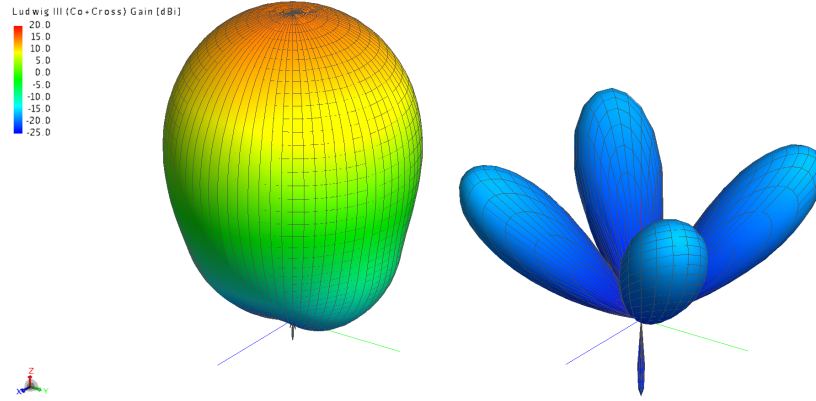


Figure 2-5: Co- and cross-polarization pattern of the VeGA antenna

Figure 2-5 shows the co- and cross-polarization radiation pattern of the VeGA antenna. The cross-polarization is, in most cases, desired to be small in magnitude compared to the co-polarization. In the figure the cross-polarization pattern is enlarged for better visualization. For the VeGA antenna the cross-polarization pattern resembles a shamrock. This shape can be best observed in the form of a polar radiation pattern as shown in chapter 3.4.

2.1.1 Field Regions

The space around an antenna is categorized into three sections. The direct space around the antenna is called the reactive near field, after which comes the radiating near field and the far field.

The radiation pattern is calculated or measured in the far field as the pattern remains constant in this region, which means it does not change as the distance increases. The transition between the field regions is gradual and their extent depends on the wavelength λ . [4](p. 32)

$$R_1 = 0.62 \sqrt{\frac{D_A^3}{\lambda}} \quad (2.1)$$

$$R_2 = 2 \frac{D_A^2}{\lambda} \quad \text{with} \quad \lambda = \frac{c}{f} \quad (2.2)$$

where:

- D_A = Largest dimension of the antenna [m]
- λ = Wavelength [m]
- c = Speed of light [m/s]
- f = Frequency [Hz = 1/s]

R_1 is the boundary between reactive and radiating near field and R_2 is the boundary between the radiating near field and the far field.

2.2 Directivity and Gain

An isotropic antenna radiates its power equally in all directions and is a theoretical construct. Nevertheless, it is often used as a reference to compare different antennas. The radiated power density decreases with increasing distance to the antenna and is distributed equally over the surface of a sphere. [7](p. 161) Its behaviour can be described by:

$$S_i = \frac{P_{rad}}{4\pi r^2} \quad (2.3)$$

where:

- S_i = Power density of an isotropic antenna [W/m^2]
- P_{rad} = Radiated power [W]
- r = Distance from the antenna [m]

To describe the deviation in the radiation pattern of a real antenna from an isotropic antenna the term directivity is used. The directivity is the ratio of the power density of the antenna in a given direction to the power density of an isotropic antenna. If the direction is not specified, the direction of maximum radiation intensity is implied. [4](p. 41) Both antennas have the same total radiated power.

$$D(\theta, \phi) = \frac{S(\theta, \phi)}{S_i} \quad (2.4)$$

$$= 4\pi r^2 \frac{S_{max}}{P_{rad}} \quad (2.5)$$

where:

- $D(\theta, \phi)$ = Directivity in a given direction [dimensionless]
- $S(\theta, \phi)$ = Power density in a given direction [W/m^2]
- S_{max} = Maximum power density [W/m^2]
- S_i = Power density of an isotropic antenna [W/m^2]
- r = Distance from the antenna [m]
- P_{rad} = Radiated power [W]

Some of the power fed into the antenna is lost due to finite conductivity of the an-

tenna as well as through absorption in lossy dielectric materials. These losses can be expressed via the efficiency factor η_A or with the relation of radiated power to input power as follows. [7](p. 168-169)

$$\eta_A = \eta_c \eta_d \quad (2.6)$$

$$= \frac{P_{rad}}{P_{in}} = \frac{P_{rad}}{P_{rad} + P_{loss}} \quad (2.7)$$

where:

η_A = Radiated antenna efficiency [dimensionless]

η_c = Conduction efficiency [dimensionless]

η_d = Dielectric efficiency [dimensionless]

P_{in} = Input power [W]

P_{loss} = Power dissipation [W]

This equation does not take into account the reflection losses due to mismatches of the transmission line and the antenna. The total efficiency is $\eta_0 = \eta_r \eta_c \eta_d$ and is also dimensionless. If appropriate measures are taken, the reflection losses can be negligibly small. Therefore, the antenna efficiency is usually reduced to equation 2.6 and given in percent. [4](p.60-61)

If the above losses are taken into account, the antenna the term gain is used. It is defined as follows and usually given in dB or dBi, when the isotropic antenna is used as a reference. [7](p. 169)

$$G = \eta_A D \quad (2.8)$$

$$G_{dBi} = 10 \log_{10} G \quad (2.9)$$

where:

G = Gain [dimensionless]

G_{dBi} = Gain [dBi]

If the reflection efficiency η_r is included in the calculation, the term realized gain is used. [4](p. 63)

2.3 Polarization Loss Factor

If a horizontally polarized signal is received by a horizontally polarized antenna the complete signal will be received. If the receiving antenna is misaligned in relation to the polarization of the signal, losses will occur due to polarization mismatch. Therefore, there will be a percentage of the transmitted power which can not be coupled into the receiving antenna. The term polarization loss factor describes this behaviour. [4](p.

71)

$$PLF = |\vec{\rho}_w \cdot \vec{\rho}_a|^2 \quad (2.10)$$

$$= |\cos^2(\psi)| \quad \text{with } 0 \leq \psi \leq 90 \quad (2.11)$$

$$PLF_{dB} = |20 \log_{10} \cos(\psi)| \quad (2.12)$$

where:

PLF = Polarization Loss Factor [dimensionless]

$\vec{\rho}_w$ = unity vector of the electrical field of the incoming wave

$\vec{\rho}_a$ = unity vector of the electrical field of the receiving antenna

ψ = Angular deviation between incoming and received polarization [deg]

PLF_{dB} = Polarization Loss Factor [dB]

The polarization loss factor is also known as polarization mismatch. If $\psi = 0^\circ$ the antennas are aligned perfectly and $PLF = 0$ dB. For a deviation of 90° the polarizations are opposites of each other. This means, no power will be received as PLF would be ∞ dB.

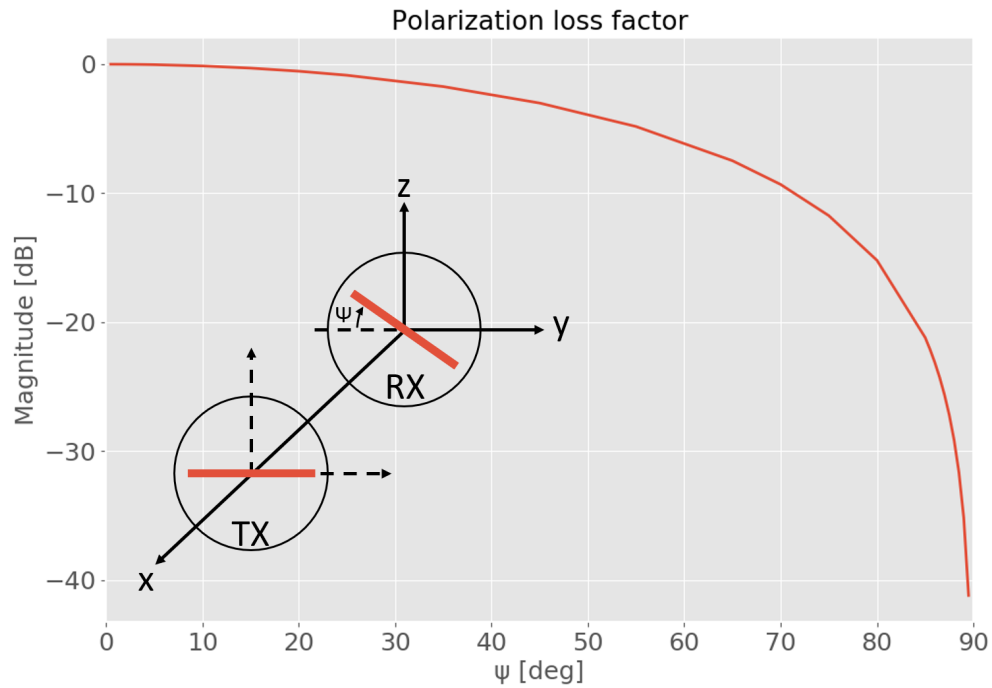


Figure 2-6: Calculated polarization loss factor over ψ

Figure 2-6 shows the calculated polarization loss factor over ψ as well as a sketch to show the previously described angular offset between the antennas. In the figure transmitter (Tx) and receiver (Rx) are used to distinguish between the antennas.

2.4 Waveguides and Modes

The term waveguide describes a structure, which can transport electromagnetic energy waves between two points. In this thesis the term waveguide refers to a hollow structure made out of a conductive material. These types of waveguides are mostly used for horn and reflector antennas. [7](p. 354)

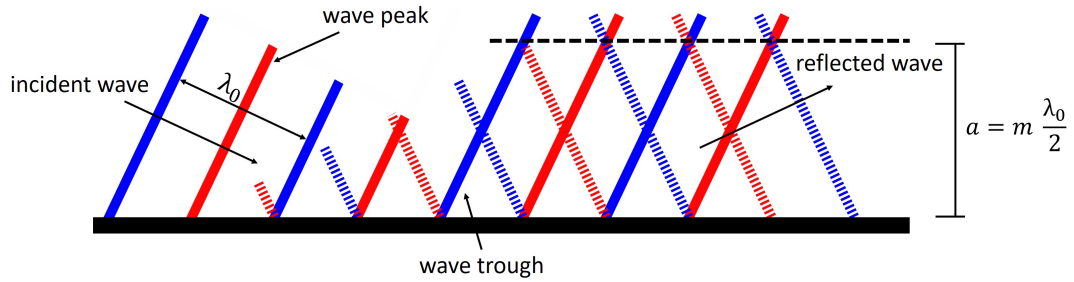


Figure 2-7: Depiction of the wave propagation in waveguides (top view) with $m = 1, 2, 3, \dots$ (adapted from [5])

When a plane electromagnetic wave is coupled into a rectangular waveguide it is reflected at its inner walls. With the correct dimensions as depicted above the reflected wave interferes with the incident wave. This produces an interference pattern with maxima and minima. This wave field propagates along the waveguide. The incident angle of the wave can be within $0^\circ < \Phi < 90^\circ$. If 90° are exceeded no propagation will take place. In addition to this a transmission in waveguides can only take place starting from the respective cut-off-frequency f_c , which depends on the dimensions of the waveguide. [5](p. 75-76)

Different mode forms can be found in a waveguide of which some are depicted in figure 2-8. They are all based on one of two possible types. The transverse electric (TE) mode has its electric field lines across the z -direction and the magnetic field pointing in the propagation direction. For the transverse magnetic (TM) mode the opposite is the case. In this case the magnetic field lines are across the propagation direction and the electric field component points in z -direction. Both mode types can take on different forms in waveguides and can exist simultaneously. The forms are differentiated by including two indices in their descriptive name leading to the denomination TE_{mn} and TM_{mn} . For example the transverse electric mode TE_{10} with $m = 1$ and $n = 0$ is called the fundamental mode.

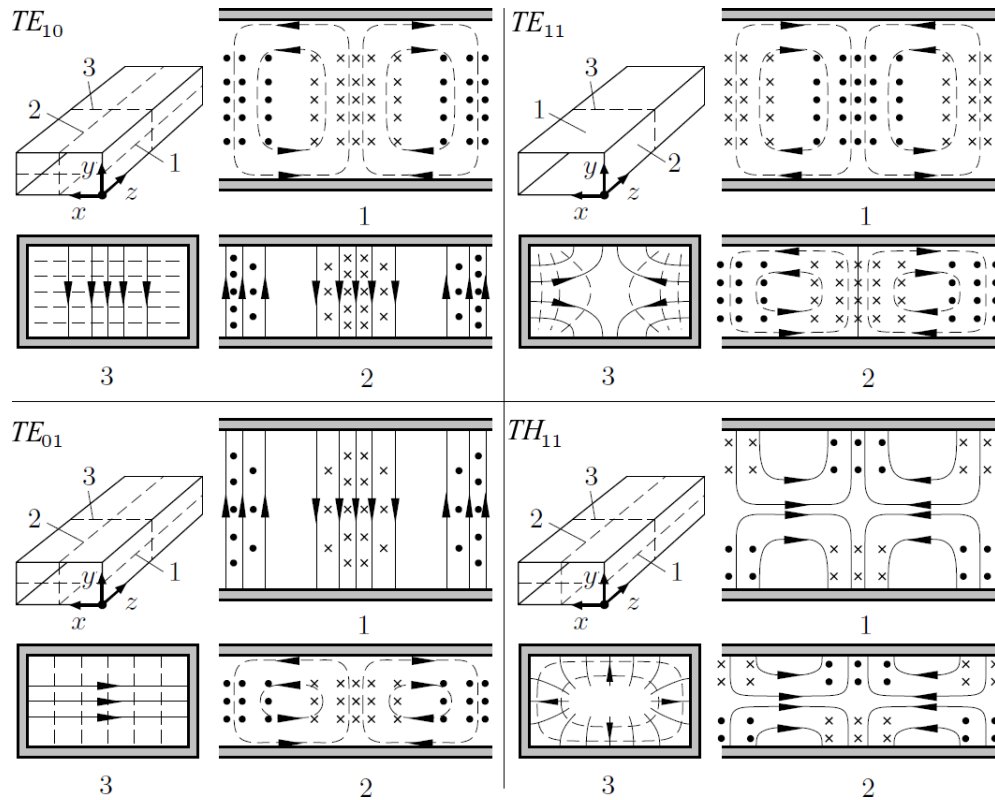


Figure 2-8: Depiction of the field lines within a rectangular waveguide where the drawn through lines represent the electric field and the dashed lines the magnetic field. (adapted from [6](p. 332))

The different mode forms in a rectangular waveguide are illustrated as shown in figure 2-8. Where, based on view number 3, m = the number of maxima along the broad side and n = the number of maxima along the narrow side of the waveguide. Circular waveguides exist as well but their mode forms vary from those of a rectangular waveguide. Some examples are given in [7](p.127).

If a waveform has magnetic and electric parts pointing towards the propagation direction in the waveguide the mode is classified as a hybrid mode. Depending on which of both fields is stronger these modes are called HE or EH modes. HE modes lean more towards a TE mode whereas EH modes resemble TM modes. [18](p. 364)

If such a hybrid mode is fed into a horn antenna with a Gaussian profile and corrugations a so-called Gaussian beam mode can be transmitted. [19] (p. 20) The field intensity profile of this mode conforms in good approximation to a Gaussian profile.

2.5 Transmission Lines

To connect an antenna to a source (or a receiver) transmission lines are needed. These can for example be coaxial cables or waveguides. The characteristics of transmission lines will be explained on a coaxial line as shown below.

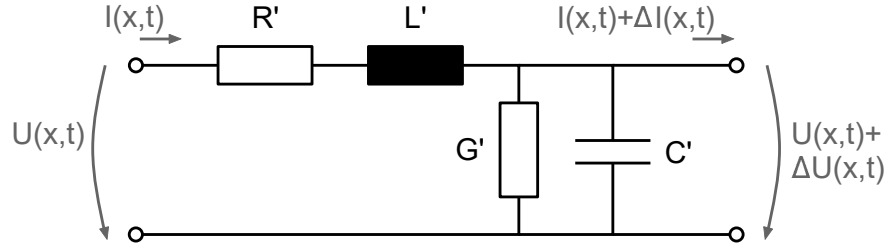


Figure 2-9: Equivalent circuit diagram of a small section of a coaxial line (adapted from [7](p. 157))

The characteristic variables can be described as follows:

- R' = resistance of the transmission line [Ω/m]
- L' = inductance of the transmission line [H/m]
- G' = isolation between the conducting wires of the transmission line [S/m]
- C' = capacitance between both conductor lines [F/m]

With these parameters the following equations can be obtained. [20]

$$-\frac{\partial U(x,t)}{\partial x} = R'I(x,t) + L'\frac{\partial I(x,t)}{\partial t} \quad (2.13)$$

$$-\frac{\partial I(x,t)}{\partial x} = G'U(x,t) + C'\frac{\partial U(x,t)}{\partial t} \quad (2.14)$$

Subsequently, the telegrapher's equation can be derived from 2.13 and 2.14 for both voltage and current. The results are partial second-order differential equations, in which $U = U(x,t)$ and $I = I(x,t)$. They describe the voltage and current intensities as functions of time and place on the transmission line.

$$\frac{\partial^2 U}{\partial x^2} = R'G'U + (R'C' + G'L')\frac{\partial U}{\partial t} + L'C'\frac{\partial^2 U}{\partial t^2} \quad (2.15)$$

$$\frac{\partial^2 I}{\partial x^2} = R'G'I + (R'C' + G'L')\frac{\partial I}{\partial t} + L'C'\frac{\partial^2 I}{\partial t^2} \quad (2.16)$$

Equations 2.13 and 2.14 are transformed into the frequency domain and combined into a partial differential equation of second-order. In this case $U = U(x, j\omega)$.

$$\frac{\partial^2 U}{\partial x^2} = (R' + j\omega L')(G' + j\omega C')U \quad (2.17)$$

$$= \gamma^2 U \quad (2.18)$$

The solutions of 2.17 describe the idea of a forward and a reflected wave on a transmission line in the form $U = A \cdot e^{-\gamma x} + B \cdot e^{\gamma x}$ and $I = s \cdot (A \cdot e^{-\gamma x} - B \cdot e^{\gamma x})$. The results for the voltage and current intensities are related via the factor $s = \gamma / (R' + j\omega L')$. With this relation the complex wave impedance \underline{Z}_0 of the transmission line can be determined. [6](p. 360)

$$\underline{Z}_0 = \frac{U}{I} = \frac{R' + j\omega L'}{\gamma} \quad (2.19)$$

$$= \sqrt{\frac{R' + j\omega L'}{G' + j\omega C'}} \quad (2.20)$$

$$\approx \sqrt{\frac{j\omega L'}{j\omega C'}} = \sqrt{\frac{L'}{C'}} \quad \text{for high frequencies} \quad (2.21)$$

When the load at the end of the transmission line has the same impedance as the wave impedance ($\underline{Z}_L = \underline{Z}_0$) the signal will be absorbed into the load and no reflection will take place at their connection. This is referred to as impedance matching. If no load is connected to the transmission line ($\underline{Z}_L = 0$) or if the transmission line is short-circuited ($\underline{Z}_L = \infty$) total reflection will take place. The relation between \underline{Z}_L and \underline{Z}_0 is known as the complex reflection coefficient $\underline{\Gamma}$. [6](p. 362)

$$\underline{\Gamma} = \frac{\underline{Z}_L - \underline{Z}_0}{\underline{Z}_L + \underline{Z}_0} = \frac{V_{refl}}{V_{inci}} \quad (2.22)$$

$\underline{\Gamma}$ can also be described as the ratio of the amplitudes of the reflected voltage wave V_{ref} to the incident voltage wave V_{inci} . [12](p. 57)

2.6 S-Parameters

When working with high frequencies it is common to describe the behaviour for electrical devices such as transmission lines or amplifiers by so-called s-parameters. In this context the electrical devices are called n-port networks. N indicates the number of interfaces where electro magnetic waves enter and exit the network. To fully describe their behaviour a set of s-parameters is used. Each s-parameter is defined as the ratio of complex voltages from the reflected and incident wave at the respective port combination.

To differentiate clearly between the s-parameters indices are used. All \underline{S}_{ij} are listed in the scattering matrix \underline{S} , which describes all reflections and transmissions of the network.

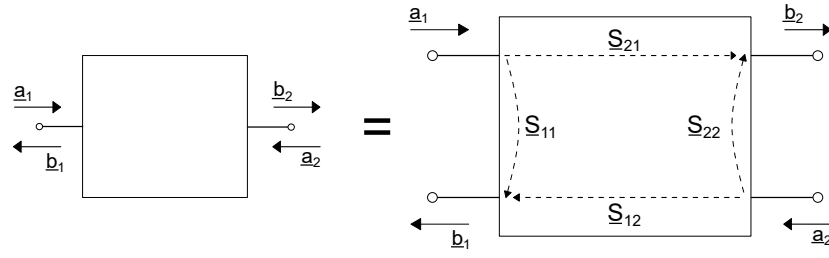


Figure 2-10: Depiction of the s-parameters of a 2-port network with the incident and reflected waves

Figure 2-10 shows the visualization of a 2-port network with its respective reflections and transmissions. All waves \underline{a}_k and \underline{b}_l are complex. The scattering matrix of the network is shown in equation 2.23 and can be used to link the waves going into and leaving the network as follows.

$$\underline{S} = \begin{bmatrix} \underline{S}_{11} & \underline{S}_{12} \\ \underline{S}_{21} & \underline{S}_{22} \end{bmatrix} \quad (2.23)$$

$$\begin{pmatrix} \underline{b}_1 \\ \underline{b}_2 \end{pmatrix} = \begin{bmatrix} \underline{S}_{11} & \underline{S}_{12} \\ \underline{S}_{21} & \underline{S}_{22} \end{bmatrix} \begin{pmatrix} \underline{a}_1 \\ \underline{a}_2 \end{pmatrix} \quad (2.24)$$

\underline{S}_{11} is the ratio of the reflected to the incident wave at the input port of the network, while \underline{S}_{22} is the same for the output port. They are called reflection coefficients and can also be referred to as $\Gamma_{in} = \underline{S}_{11}$ and $\Gamma_{out} = \underline{S}_{22}$. \underline{S}_{21} and \underline{S}_{12} are called transmission coefficients. They represent the relation of the received voltage on port i to the voltage of the incident wave on port j. [12](p. 178)

The s-parameters are often given in dB as logarithmic values. The conversion is as follows. [12](p. 58)

$$S_{ij} = 20 \log_{10} |\underline{S}_{ij}| \text{ dB} \quad (2.25)$$

3 The VeGA Antenna

This chapter will introduce the choked gauss antenna (German: Verkürzte Gauss-Antenne) (VeGA), which was used in the following simulations and measurements. Developed in the course of several theses [8] [10] [19] for P-band, the antenna was scaled down to be able to operate in L-band. The antenna consists of two main parts. The first being the antenna flare, which is based on a choked gaussian profiled horn antenna (GPHA). The second part is the orthomode transducer (OMT), which is the feeding system of the antenna. This chapter will also address the hybrid feed network, which is needed to generate the desired signals.

As the reciprocity principle can be applied to the antenna, the antenna can be operated as a transmitting or receiving antenna with the same setup [4](p. 140). The following explanations refer to the receiving case.

3.1 Antenna Flare

The antenna flare of the VeGA antenna is based on a choked gaussian profiled horn antenna (GPHA). A GPHA consists of two components. First, the Gaussian horn profile and second, the so called antenna throat [8](p. 30). The corrugated Gaussian horn profile was chosen due to its low cross polarization and low side lobes [21](p. 1).

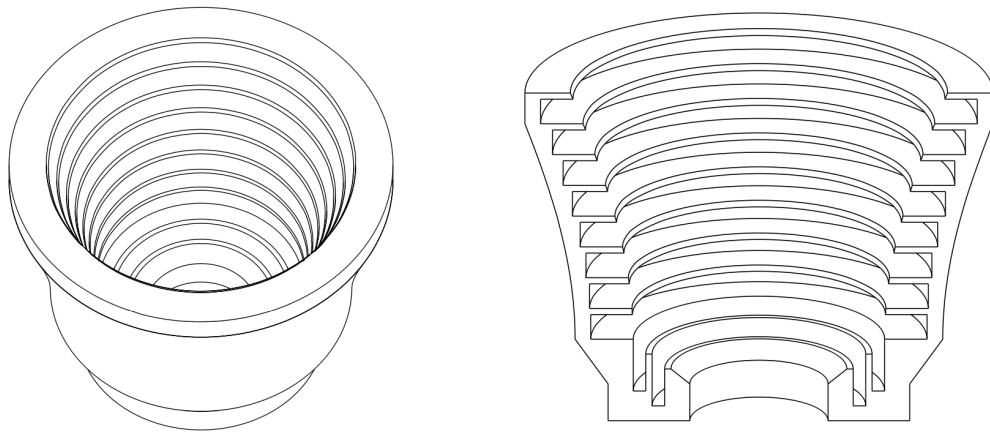


Figure 3-1: Antenna flare of the VeGA antenna [8](p. 39)

Figure 3-1 shows the developed antenna flare. The Gaussian profile shows horizontal corrugations while the antenna throat has vertical corrugations. Detailed information on the antenna flare design, such as the chosen depth for the corrugations, can be found in [8](p. 30-39).

A Gaussian beam mode is coupled from free space into the horn profile. This mode is then transformed into a hybrid mode HE_{11} by the horn profile. The antenna throats

converts the HE_{11} into a TE_{11} mode [22, p. 1505]. The TE_{11} mode is then coupled into the OMT.

3.2 Orthomode Transducer

With the OMT a dual linear polarization feeding system for the antenna was realised. This means, the feeding system has to distinct orthogonal polarization channels. These polarizations will be referred to as horizontal (H) and vertical (V) polarization from now on.

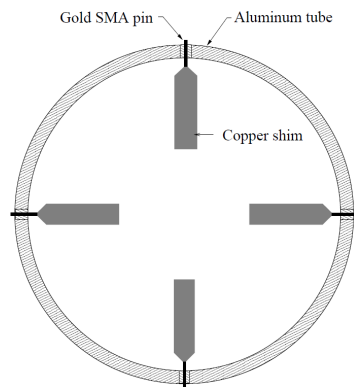


Figure 3-2: Layout of a planar OMT
(adapted from [9])

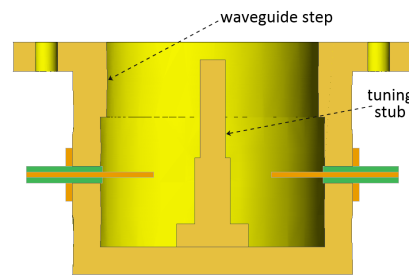


Figure 3-3: Geometry of the optimised OMT including waveguide step and tuning stub (from [10](p. 44))

Figure 3-2 shows the geometry of the OMT. Its design was chosen to be planar. For this, a printed circuit board (PCB) on which four metallic probes are arranged at 90° intervals is integrated into a circular waveguide. The OMT therefore has four output ports. With this setup, two orthogonal polarizations can be received simultaneously - each with one pair of opposing probes [10](p. 44-45).

In addition to the usual planar OMT design, a waveguide step as well as a tuning stub were implemented to further improve the OMT [10](p. 40-42).

The signals from the output ports of the OMT are passed on to the so called hybrid feed networks.

3.3 Hybrid Feed Network

To omit the intrinsic amplitude and phase imbalance of the hybrid couplers, step attenuators and phase shifters are used. The adjustment of these components is referred to as tuning and will be explained in chapter 5.2. This section will briefly discuss the construction of the hybrid feed network used in the later measurements.

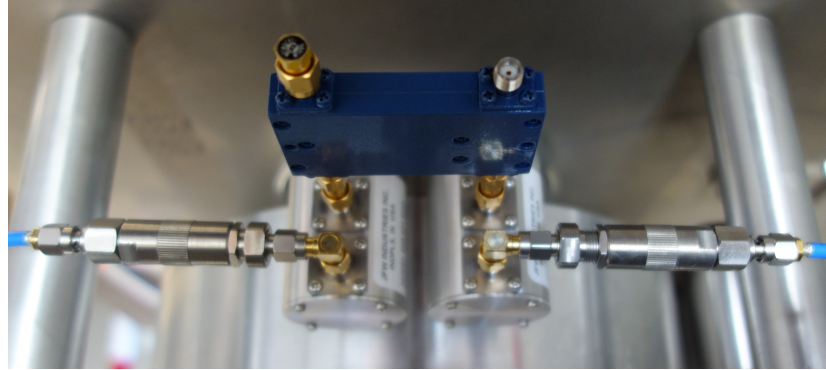
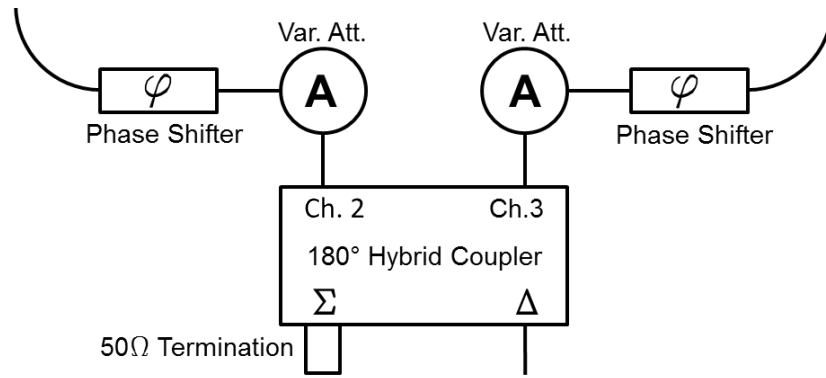


Figure 3-4: Diagram of the hybrid feed network (top, adapted from [11, p. 10]) and picture of a hybrid feed network used for measurements (bottom)

A 180° hybrid coupler has four ports. Port 1 is the sum (Σ) port, port 2 and 3 are output ports and port 4 is known as the difference or delta (Δ) port. Each of the two feed networks consists of one hybrid coupler, two step attenuators and two phase shifters. The phase shifters are connected to the output ports of the step attenuators. This assembly is then connected to the output ports of the hybrid coupler. Figure 3-4 shows the assembly of a hybrid feed network.

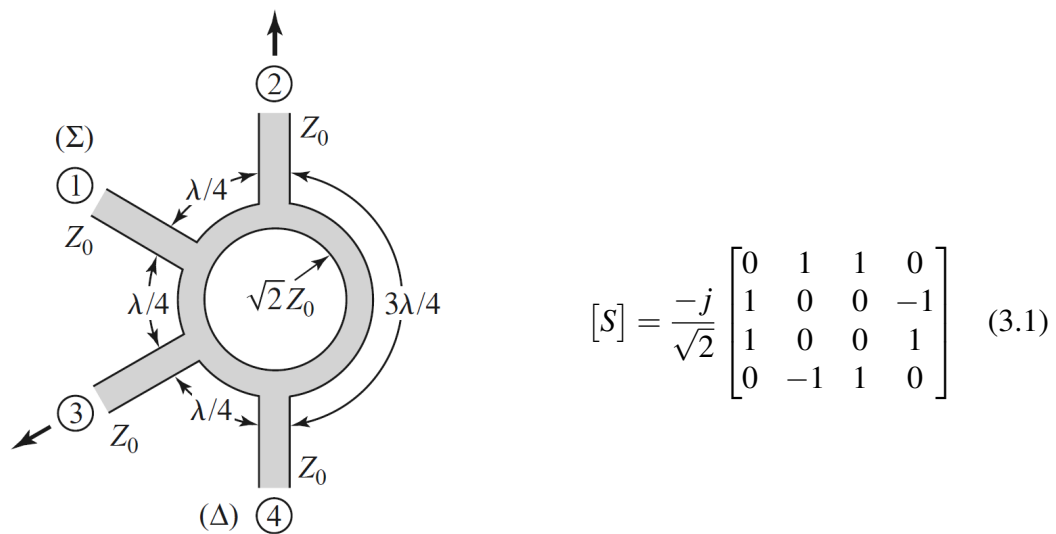


Figure 3-5: Structure of a 180° ring coupler in microstrip line or stripline form (left) and its ideal scattering matrix (right, from [12](p.363))

The structure of a hybrid coupler is shown in figure 3-5 in form of a ring or rat-race coupler. The signal is split equally between both output ports. Additionally, the hybrid coupler generates a 180° phase shift between the output ports if a signal is applied to the Δ port. The not utilised Σ port is terminated with $50\ \Omega$ to attenuate signal reflections. The coupler, when used like this, is utilised as a power divider. The signal can also be applied to the Σ port of the coupler while the Δ port is terminated. This will cause two equally split but in-phase signals at the output ports. With this method of operation the coupler is known as a power combiner.

For the VeGA antenna the hybrid couplers are used in the power divider setup. The phase shifters of a network are connected to opposing antenna output ports.

3.4 Final Design

The VeGA antenna (including the OMT) has a height of 0.75 m and a maximum diameter of 0.71 m.

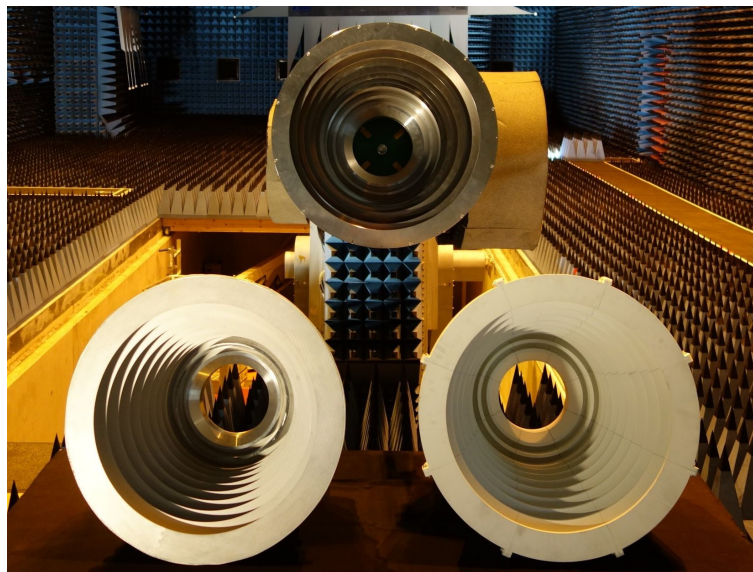


Figure 3-6: All three versions of the VeGA antenna. On top and mounted on the CTR positioner is the aluminium antenna, left is the CFK antenna and on the right is the 3D-printed antenna. (from [11](p. 7))

Additional versions of the L-band VeGA antenna flare have been produced to compare their performances in a CTR measurement campaign. An aluminium version as well as a CFK version were compared to the original 3D-printed antenna flare from [19]. To fit the production requirements the antenna model had to be altered and the later antennas therefore slightly differ from the 3D-printed antenna. The ridges between each corrugation were thinned out and the ridges inner facing sides were flattened out. In the measurement campaign the same OMT (made out of aluminium) was used for all antenna flares. Figure 3-6 shows the three antenna flares in DLR's compact test

range (CTR).

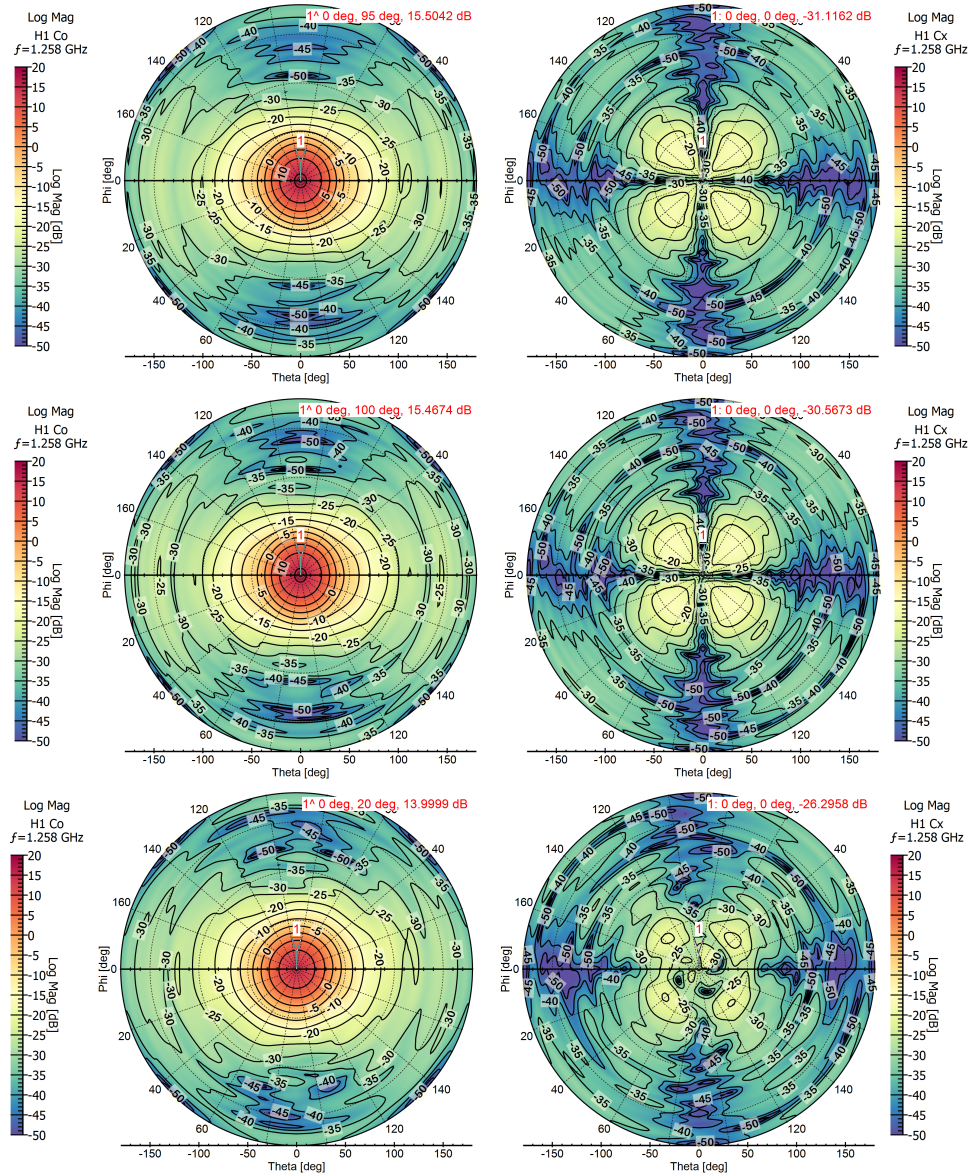


Figure 3-7: Co-polarization (left) and cross-polarization (right) of the aluminium, CFK and the 3D-printed VeGA antenna (from top to bottom, taken from [11](p. 15))

Figure 3-7 shows the measurement results for all three antennas in the form of gain patterns for both co-polarization as well as cross-polarization for the horizontal polarization channel of the antenna. The aluminium and the CFK antenna have a maximum gain in co-polarization of around 15 dB while the printed antenna model shows a deviation of around -1.5 dB in comparison. All three cross-polarization patterns show a shamrock shape but it can also be noted, that the pattern of the 3D-printed antenna deviates from the other two.

The CTR measurements shows that the aluminium and the CFK VeGA antenna both fulfil the specified requirements and have an equal performance. Due to the advantages of the CFK antenna (weight, temperature expansion behaviour and cost) this

version will be used for the prototype (and possibly the series) of the L-band calibration transponder [11](p. 22). For the measurements in this thesis, both the aluminium and the CFK antenna are used.

4 Simulation

Currently there are various antenna design and simulation tools on the market. For the simulations in this thesis the computational electromagnetic (CEM) software FEKO (version 2018.2.1) is used. The abbreviation stems from the german name "Feldberechnung für Körper mit beliebiger Oberfläche". This means, the software utilises various solution methods to analyse electromagnetic fields involving three-dimensional objects of any shape. [23](p. 20) The following paragraphs will outline the general procedure to obtain simulation results with FEKO.

Two different applications from FEKO are used for the construction and simulation of the VeGA antenna. The three-dimensional antenna geometry can be constructed in CADFEKO by either using the graphical user interface (GUI) or the application programming interface (API). As the antenna geometry is very complex, the previously developed VeGA antenna was implemented in script form using the Lua programming language. This way the antenna's (frequency) scalability was ensured and the antenna is constructed by running the script in the API. The script provided the basis for the adaptations made in this thesis. CADFEKO also provides the possibility to include transmission lines and non-radiating networks, which can be described by specifying their scattering matrix.

To start a simulation, the constructed antenna model has to be meshed to generate a discretised representation of its geometry. The resulting mesh is called simulation mesh and is made up of triangles when using the default solution method method of moments (MOM). The length of the triangle sides can be adjusted and local mesh sizes for certain areas can be defined. The smaller the triangles are the finer the geometry will be meshed. Decreasing the mesh element size will lead to a prolonged calculation time, which is why the use of fine local mesh sizes is encouraged.

The FEKO solver uses the simulation mesh to calculate the previously made requests. These simulation requests can for example be farfield, nearfield or s-parameter requests. To calculate the requests the MOM method is used. This method solves functional equation problems, in this case the Maxwell integral equations, by approximating it using a matrix equation in the frequency domain. [24](p. 1) [25](p. 1)

The results of the simulation can be viewed and analysed with the application POSTFEKO. It is possible to depict the calculated requests in various ways including Cartesian, polar and three-dimensional coordinate systems. The application is used for a first evaluation of the s-parameter results. The data is exported and plotted with the use of Python scripts to ensure the comparability between the simulation and measurement

results.

4.1 Simulation Setup

The goal of the simulations is to provide information on the changes in the farfield and nearfield radiation pattern of the VeGA antenna in dependency of different parameters. To analyse the coupling between both antennas the s-parameters are used. Using them, the reflection at the antenna ports and the inter channel coupling can also be evaluated. To reflect the actual measurement setup, which utilises hybrid feed networks, adjustments on the antenna geometry are necessary. Doing so provides the opportunity to compare the simulation to the actual measurements. It is possible to get a basic idea on the magnitude of the coupling parameters which are to be expected during the measurements. By comparing both results the validity of the simulation results can be analysed and adequately considered before future tests.

Figure 4-1 shows the simulation setup and illustrates the varied parameters. First the distance between both antennas is varied to obtain the coupling parameters dependent on the distance. Then the second antenna is rotated around its z-axis to obtain the dependency between the coupling parameters and the axis misalignment. The position and alignment of the first antenna was kept unchanged during all simulations. For the calculation of the far and near field the first antenna is used as the transmitting antenna.

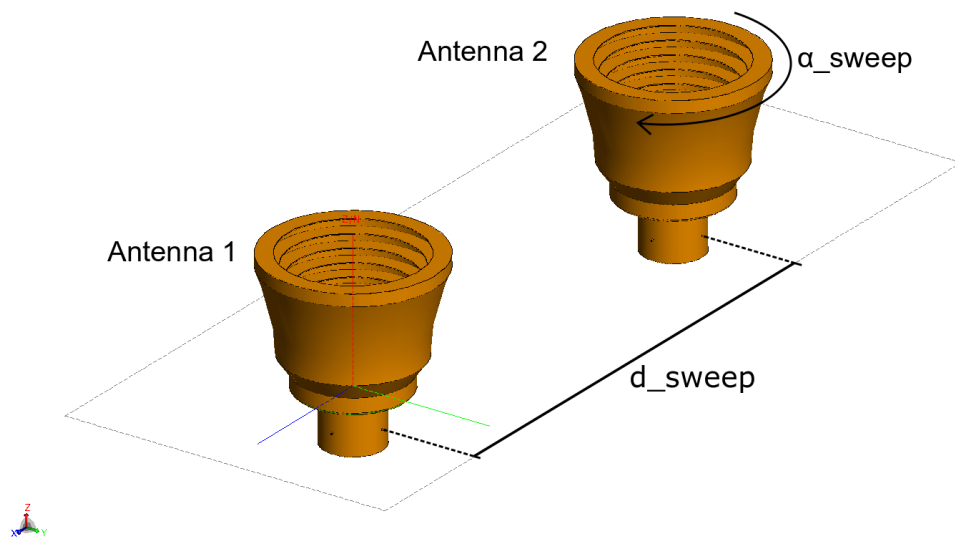


Figure 4-1: Antenna model setup

Figure 4-2 and table 4-3 clarify the relations between the polarizations of both antennas and the corresponding s-parameters. The indices of the s-parameters are based on the numbers of the feed networks corresponding to the specific polarization set. All future

uses of the s-parameters in regard to the antennas are based on this definition. The terminology co- or cross-coupling will also be used as noted in the table. For the coupling between two feed networks of one antenna the term inter-channel-coupling is used.

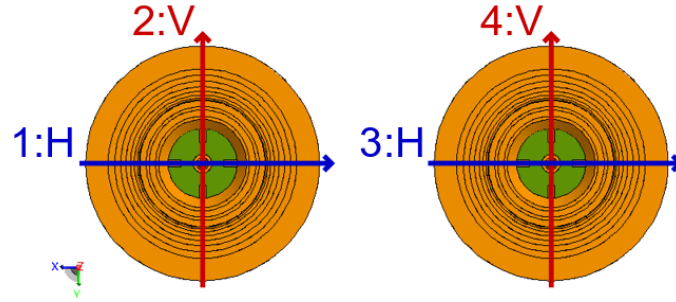


Figure 4-2: Illustration of horizontal and vertical polarizations for both antennas including the numbers of the hybrid feed networks

Polarization set	Corresponding s-parameter	Referred to as
HH	S_{31}	Co-Coupling
HV	S_{41}	Cross-Coupling
VH	S_{32}	Cross-Coupling
VV	S_{42}	Co-Coupling

Figure 4-3: Relation between polarization sets and s-parameters

In the following, the alterations on the antenna and the overall simulation setup will be described in more detail. Although the necessary changes on the antenna can be made on the three-dimensional model itself, they are implemented in the existing Lua script. This way repetitive and error-prone tasks can be automated.

The script is altered to generate a second antenna geometry, which is translated 1 m on the x-axis to reflect the intended measurement setup. By using a parameter with the name *d_sweep* to translate the second antenna, the distance between the antennas is parametrised. As it is also intended to investigate the influence of the rotation of the second antenna on the antenna coupling, another parameter called *α_sweep* is integrated.

The former antenna model utilises waveguide ports as signal sources at each of the four antenna ports. To adapt the simulation to the measurement setup the hybrid couplers are included in the form of non-radiating networks using their ideal scattering matrix (see 3.1). Like an actual hybrid coupler the network has four output ports, which, based on the denomination in FEKO, are referred to as terminals in this chapter. To connect the terminals to the respective antenna ports the port geometries have to be modified.

They are adapted to allow the use of edgeports, which can be attached to terminals. This process will not be described here but can be found in the source code of the Lua file on the enclosed CD.

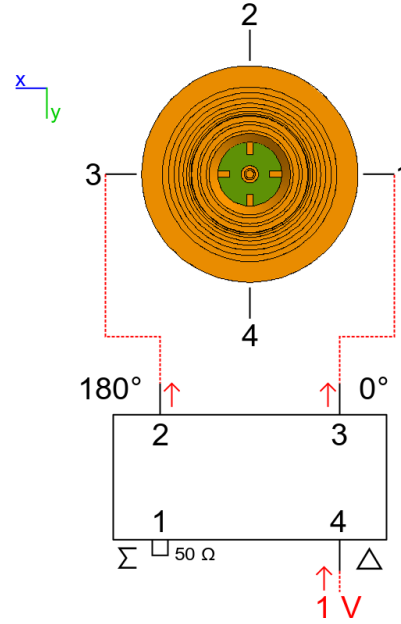


Figure 4-4: Connection of hybrid coupler 1 to antenna 1

To represent the actual antenna setup each opposing pair of antenna ports is connected to one hybrid coupler. This way two hybrid couplers per antenna are used. Figure 4-4 shows the connection of the first hybrid coupler to the transmitting antenna. This procedure is repeated for the rest of the antenna port sets on both antennas. This generates the connection setup shown in table 4-1.

Hybrid Coupler Port	Phase shift	Antenna	Antenna Port
HC1.2	180°	1	3
HC1.3	0°		1
HC2.2	180°		4
HC2.3	0°		2
HC3.2	180°	2	7
HC3.3	0°		5
HC4.2	180°		8
HC4.3	0°		6

Table 4-1: Port mapping between hybrid couplers and antennas

A horizontal polarization of the first antenna is obtained by exciting the Δ terminal of the first hybrid coupler, while the use of the second hybrid coupler results in a vertical polarization. For the calculation of the field patterns all open terminals, meaning every unused Δ and all Σ terminals, have to be terminated with $50\ \Omega$. This is done using one-port networks with $S_{11} = 0$, which is equivalent to an ideal termination [26](p. 71). A

view of the networks for one of the field pattern simulations is included in appendix A.1-1. For the calculation of the s-parameters all Σ ports have to be terminated.

The far field the field points, which shall be calculated, are located on a sphere. It is divided in increments of 1° for ϕ and θ . For the simulation of the near field a cuboid shape is chosen. Its height and width are constant over the measurement series for d_sweep . As the distance between the antennas increases with each simulation, the length of the cuboid changes accordingly. A visualisation of the requested fields is included in appendix A.1-2.

A multiport s-parameter request is made to compute the various parameter combinations. All Δ terminals of the hybrid couplers are included in this request. Ultimately, the values calculated for the Δ ports are of interest to make statements regarding the reflection at the ports themselves as well as the co- and cross-coupling between the antennas. In addition to that, the inter channel coupling of the antennas can be analysed.

The antenna geometry is meshed before the requests are calculated. Especially for the antenna ports a fine mesh is important. Therefore, the meshsize for the edgeports is set at 1×10^{-3} m. The outer structure of the antenna is meshed with $outer_mesh = \frac{\lambda}{5}$ m with $f_0 = 1.2575$ GHz. Doing so reduces the simulation time while still providing adequately accurate results. The rest of the geometry, particularly the corrugated inside, is meshed using the advanced mesh settings auto-generating a finer mesh.

An application plug-in for CADFEKO allows the consecutive calculation of setups with changing geometries. The plugin can also be used to combine the results in POSTFEKO.

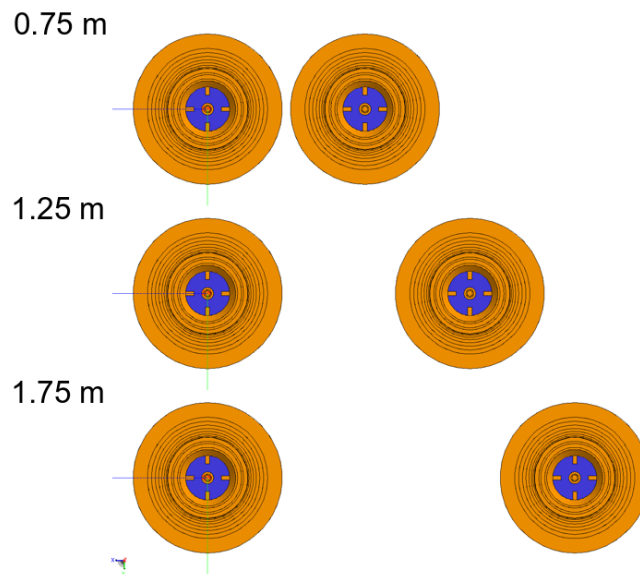


Figure 4-5: Visualization of different distances between the antennas

For a better understanding and visualization of the parameter d_sweep figure 4-5 is included in this chapter. The distance is measured between the center points of the antennas. The centres are located on the tuning stubs inside of the OMTs. This is indicated above by the coordinate system and can also be seen in figure 4-1. For simplicity, this distance will from now on be referred to as the distance between the antennas instead of the distance between the antenna centres.

As the distance between the antennas has a significant influence on the transponder design, the goal is to minimise this distance as much as possible. Thus, d_sweep is varied to have finer intervals while being in close proximity of the first antenna. For α_sweep a greater effect for the cross-coupling is expected for small changes in the alignment of the antennas. Therefore, 0.1° intervals are chosen for the first degree, continuing with 0.5° steps until a 5° rotation is reached. While one of the two parameters is varied the other one is set to a definite value. There is no rotation ($\alpha_sweep = 0^\circ$) of the second antenna while the distance is varied. D_sweep is set to 1 m during the rotation of the second antenna.

For each parameter step a new CADFEKO file is generated and saved in the output directory. Table 4-2 lists all values of α_sweep and d_sweep , which are simulated. All simulations are done for $f_0 = 1.2575$ GHz.

α_sweep (deg)	d_sweep (m)	
0.00	0.90	0.75
0.10	1.00	0.85
0.20	1.50	0.95
0.30	2.00	1.00
0.40	2.50	1.25
0.50	3.00	1.5
0.60	3.50	1.75
0.70	4.00	2.00
0.80	4.50	2.25
	5.00	2.75
		3.00

Table 4-2: Values for both sweep parameters

4.2 Simulation Results

In this section the results of the various simulations are discussed. The results of the simulations with a single antenna are presented first to provide a comparison between the simulation and CTR measurements of a single VeGA antenna. This way, the quality of the simulation can be crosschecked by means of measurements. Subsequently, the results of the double antenna setup for the distance variation and the rotation of the second antenna are discussed.

4.2.1 Single Antenna

The simulation results are compared to previously conducted CTR measurements. As only a single antenna was measured in the CTR, the simulation setup contains a single antenna as well. The parameters are simulated in a frequency range of 995 MHz to 1.505 GHz in increments of 7.5 MHz. This allows a good comparison for both magnitude as well as overall trend of the frequency dependent s-parameters. In the following the reflection parameters are referred to as S_{11} and S_{22} based on the definition in chapter 2.6 and expressed in dB as defined in equation 2.25. The inter-channel coupling S_{21} and S_{12} describes the coupling between the two channels of the antenna analog to the definition of the transmission coefficients. In addition to the s-parameters, the far and near field of the single antenna are simulated.

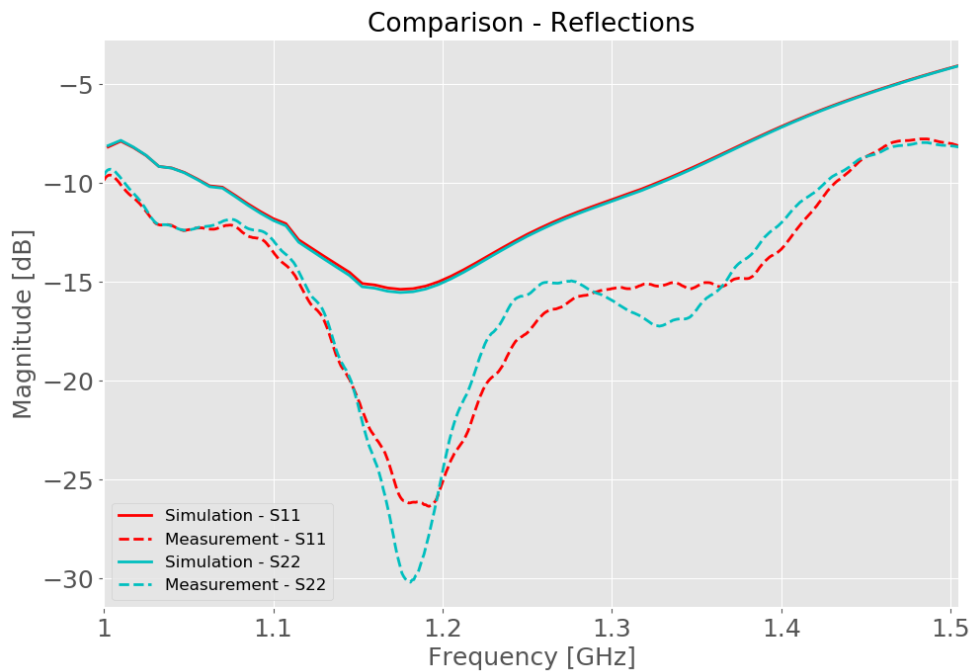


Figure 4-6: Reflections for a single antenna in comparison to the reflection of the CTR measurement as a function of the frequency

Figure 4-6 shows the reflections at the input ports of the feed networks of a single

antenna for both channels. In addition to this, the results of the CTR measurement campaign are included as dashed lines. A similar trend can be seen for both results, whereas the measurement shows lower values throughout the range of measurement. Especially the dip at around 1.18 GHz is significantly lower for the measured antenna.

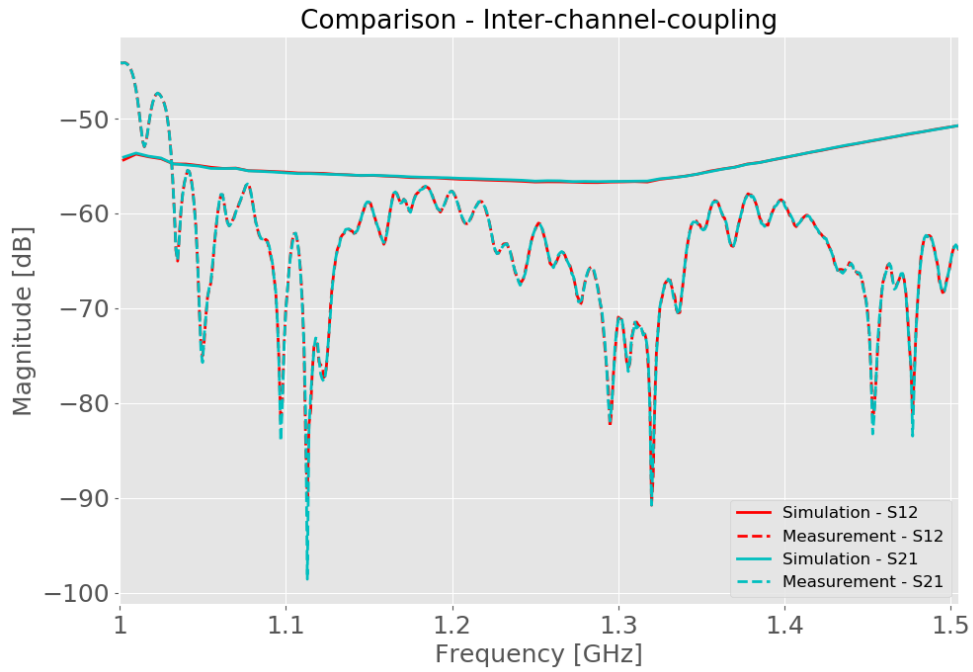


Figure 4-7: Inter-channel-coupling for a single antenna in comparison to the CTR results as a function of the frequency

The results of the simulation as well as the CTR measurement for the inter-channel-coupling are shown in figure 4-7. While the measured values show fluctuations, the simulation delivered a very stable trend. Both yield a very low inter-channel-coupling in the order of -60 dB showing a good isolation of the two antenna channels. Overall, the simulation and the measurements show a good agreement.

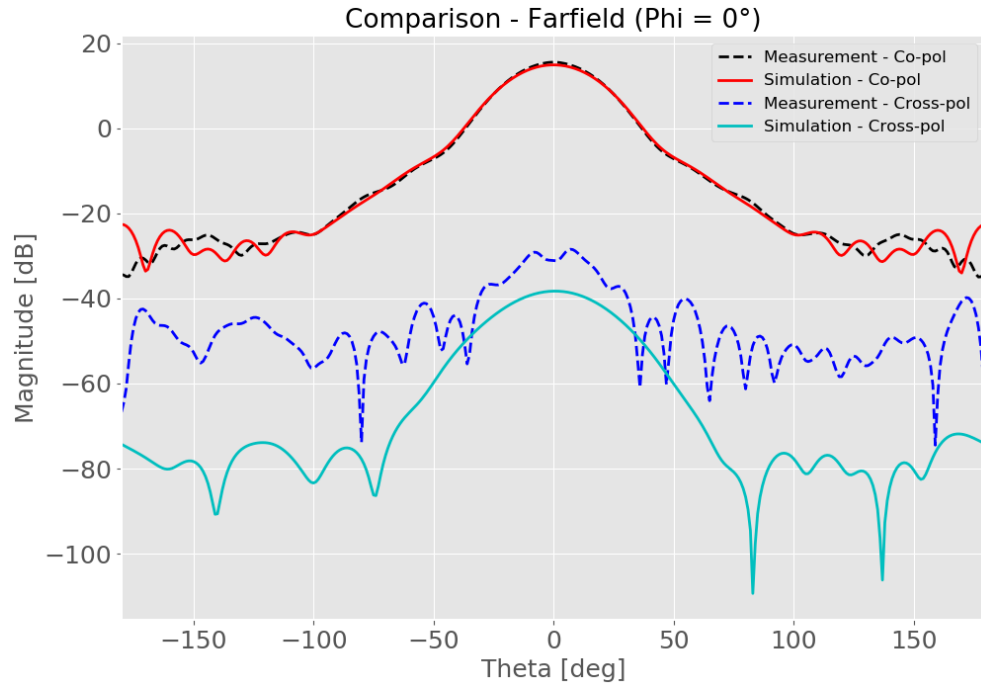


Figure 4-8: Gain pattern at $\phi = 0^\circ$ in co- and cross-polarization of the simulation and measurement

Figure 4-8 shows a cut through the gain pattern at $\phi = 0^\circ$ for both co- and cross-polarization of the antenna. The pattern for the co-polarization is in very good agreement with the measured pattern. Small deviations within the main lobe region can be seen. The maximum gain in co-polarization for both antennas lies as $\theta = 0^\circ$ and is 14.9 dB in the simulations and 15.5 dB in the measurement. For the cross-polarization the simulated values at $\theta = 0^\circ$ are -38.3 dB and -28.5 dB for the measurement.

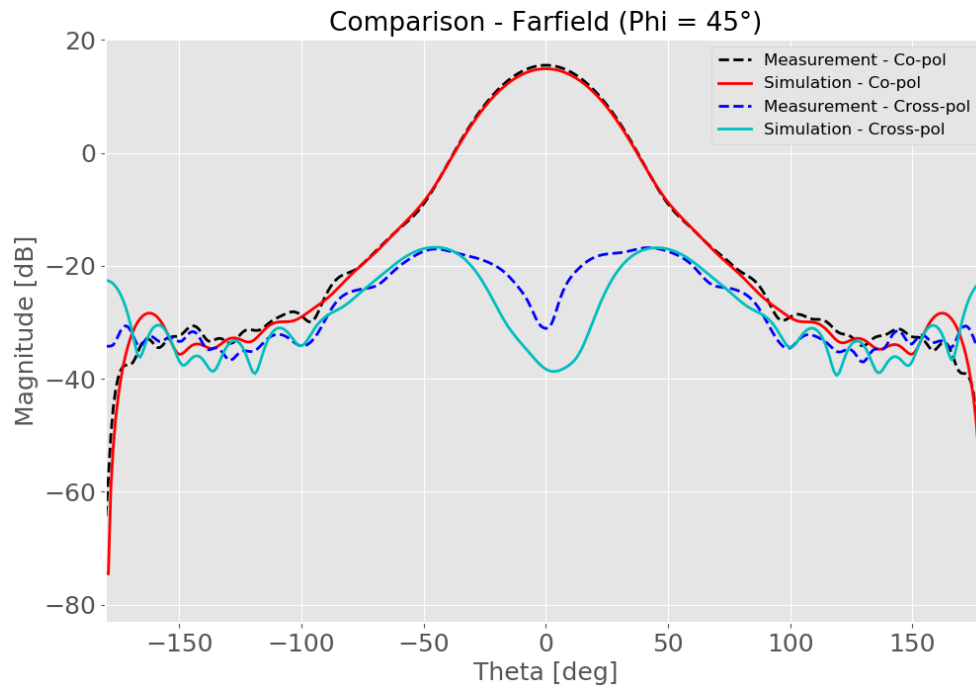


Figure 4-9: Gain pattern at $\phi = 45^\circ$ in co- and cross-polarization of the simulation and measurement

This graph shows the cuts through the gain pattern at $\phi = 45^\circ$. As can be seen in chapter 2.1 in figure 2-5 the cross-polarization pattern of the VeGA antenna has a shamrock shape and its maxima are located at $\phi = 45^\circ \pm n \cdot 90^\circ$ with $n = 1, 2, 3$. The pattern shown in figure 4-9 therefore shows the worst case for the cross-polarization. Similar trends for both results can be observed. Again the most noticeable difference can be found at $\theta = 0^\circ$ of the cross-polarization. There is a difference of around 7 dB between the measurement and the simulation.

Although small deviations can be found between the simulated and measured values, the simulation delivers acceptable results and is considered to be valid. The simulated s-parameters are within the same range and show similar trends as the measurement results for the reflections and inter-channel-coupling. The simulated gain patterns follow the measurement trend as well. Overall, the simulation showed a better cross-polarization than the measurements, which can be attributed to the ideal conditions of the simulation. In general, the results show a good representation of the actual antenna in the simulation. This confirms the use of the simulation model as a valid basis for the following simulations.

4.2.2 Double Antenna Setup

This section will discuss the co- and cross-coupling of the double antenna setup.

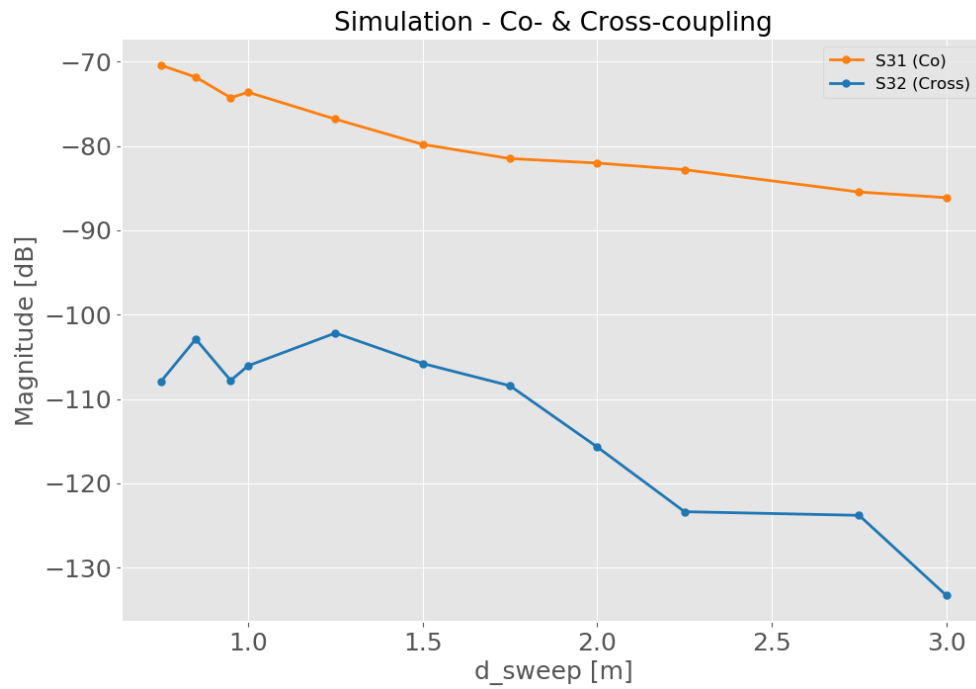


Figure 4-10: Co- and cross-coupling for f_0 over d_{sweep}

Figure 4-10 shows the co-coupling between both antennas. The behaviour of both coupling coefficients was expected to be equal as the simulation is performed without any additional objects in their proximity. For an increasing distance the coupling is expected to decrease accordingly. In the plot the same trend can be observed. Both values for the co-coupling coefficients are within the same order of magnitude. The maximum difference between both magnitudes is approximately 4 dB at a distance of 3 m. Overall, this result provides a good first estimate of the magnitude, which can be expected during the measurements.

The behaviour of the cross-coupling is presumed to be in accordance with the co-coupling. However, the order of magnitude is expected to be lower due to the mismatch of the transmitted polarization and orientation of the receiving channel.

As can be seen in figure 4-10 the results for both cross-coupling s-parameters are similar. Their values have a maximum difference of around 6.6 dB. As the results are within the range of -100 dB to -130 dB the difference could be attributed to the finite accuracy of the simulation, which would also account for the fluctuation of the parameters. It can be noted that the increasing of the distance affects both the co- as well as the cross-coupling in the same way. This means, the behaviour is in line with the expectations.

In addition to the co- and cross-coupling, the simulation showed an average magnitude of -13.5 dB for the reflection coefficients. The inter-channel-coupling is -59.5 dB on average.

To investigate the effect of a misalignment of the polarization directions the second antenna was rotated clockwise around its center axis. As the majority of the effect for the cross-coupling was expected for small angular changes, the simulation was done for a rotation of up to 5° . Ultimately, a continued rotation of the second antenna will cause the cross-coupling values to converge to the co-coupling values and vice versa.

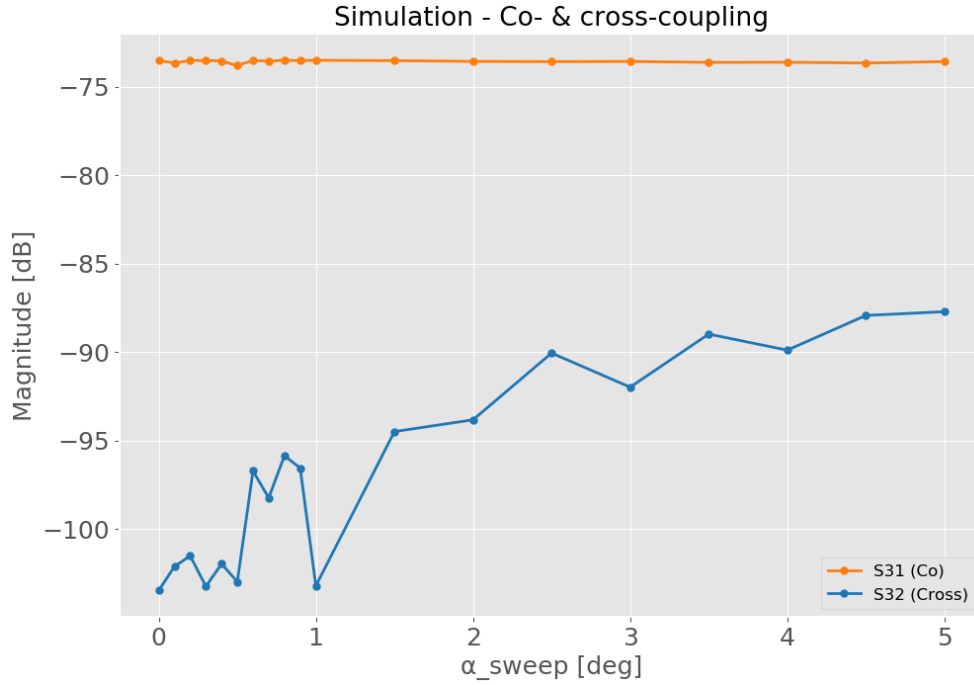


Figure 4-11: Co- and cross-coupling for f_0 over α_{sweep}

Overall, figure 4-11 shows the expected behaviour. The magnitude of the co-coupling parameters does not show any change in the first 5° , while the cross-coupling magnitude increases noticeably. The graph shows several values before 0.8° which currently can not be explained but are suspected to be outliers. Nevertheless, the trend is as expected for the cross-coupling of the antenna.

The next graphs show a comparison between the gain pattern of the single antenna with different variations of the double antenna setup for both co-and cross-polarization. Referring to the view shown in figure 4-1 the second antenna is located on the right side of the stationary antenna. Due to the definition of the spherical coordinate system this side is associated with negative values of θ .

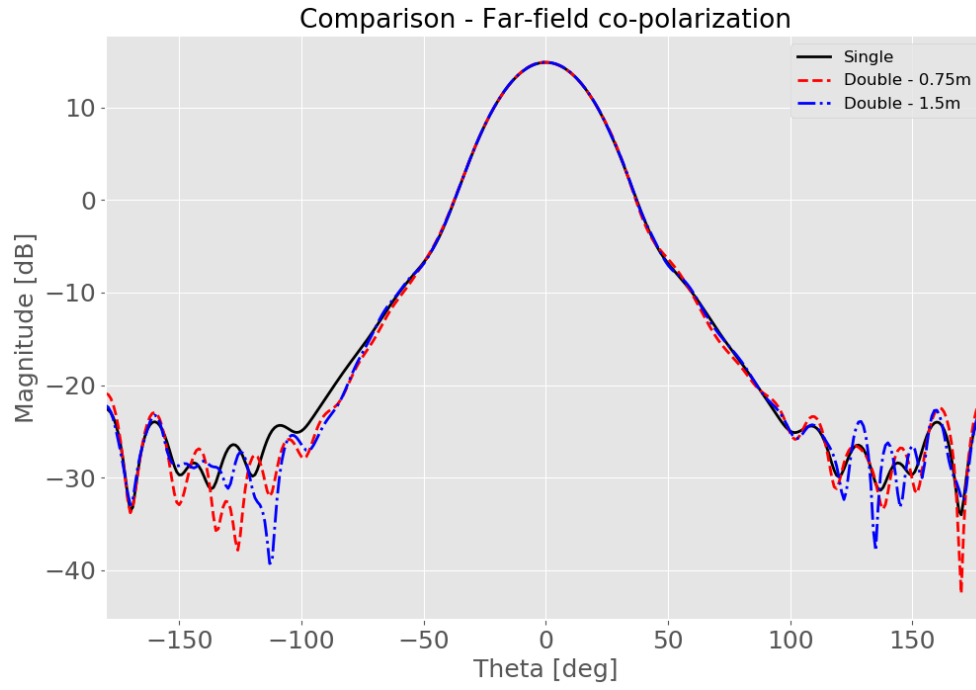


Figure 4-12: Comparison of different co-polarization gain patterns

The influence of the second antenna structure was thought to be the greatest for small distances and therefore maximal at 0.75 m. To visualize the effect for an increased distance a second graph at $d_{sweep} = 1.5$ m is included. Figure 4-12 shows the co-polarization gain pattern of the stationary antenna. The maximum gain remains at the same magnitude and at $\phi = 0^\circ$ and $\theta = 0^\circ$.

The second antenna generates small asymmetries in the regions of the side- and back lobes. In the main lobe region the pattern is almost identical and thus it can be concluded that the second antenna has no negative effect on the pattern. The sidelobes of the gain pattern are within the same order of magnitude for both distances and are still very low compared to the main beam.

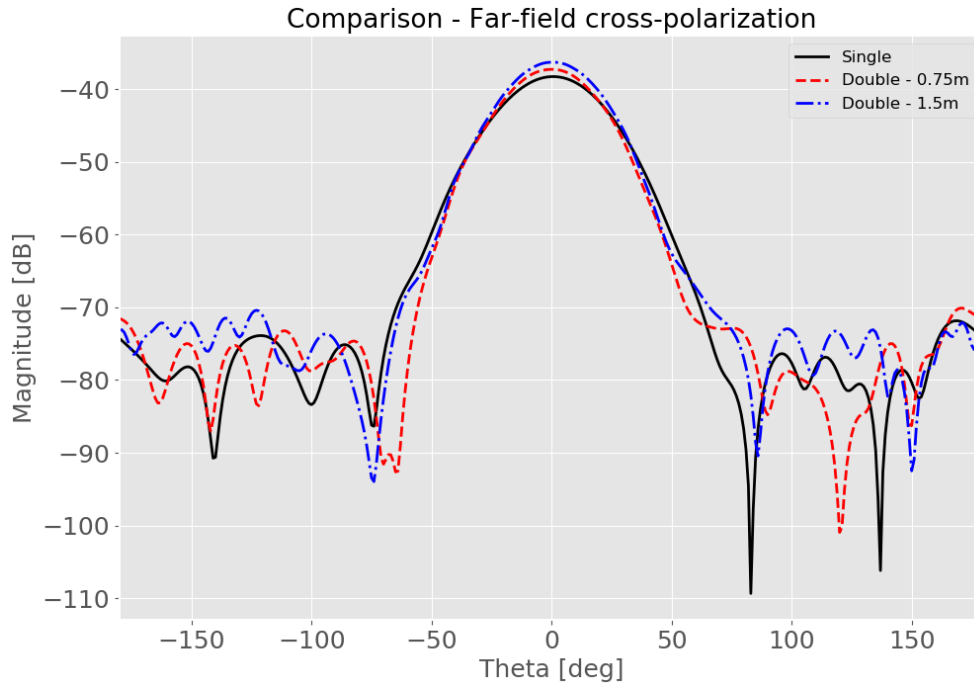


Figure 4-13: Comparison of different cross-polarization gain patterns

The corresponding measurement results of the cross-polarization are shown in figure 4-13. The maximum of the main beam of the cross-polarization increases in magnitude by 1 dB for a distance of 0.75 m and by around 2 dB for a distance of 1.5 m. Overall, the influence of the second antenna geometry is more noticeable in the cross-polarization than in the co-polarization pattern. Taking into account the order of magnitude these are negligible differences.

In addition to the far field gain pattern the near field is simulated and compared to the field pattern of the single antenna. Shown in the figure 4-14 is a cut through the XY-plane at $z = 500$ mm. This is the last simulated height at which the plane still cuts through the aperture of the antenna, which reaches until $z = 529$ mm.

The lowest picture in figure 4-14 shows the simulated near field of the single antenna. The electric field is displayed in dBV/m and decreases constantly with the distance from the single antenna. The closer the second antenna is to the stationary one, the higher is the electric field generated in its aperture. Well visible for $d_{\text{sweep}} = 2.25$ m is the wave pattern caused by the second antenna geometry.

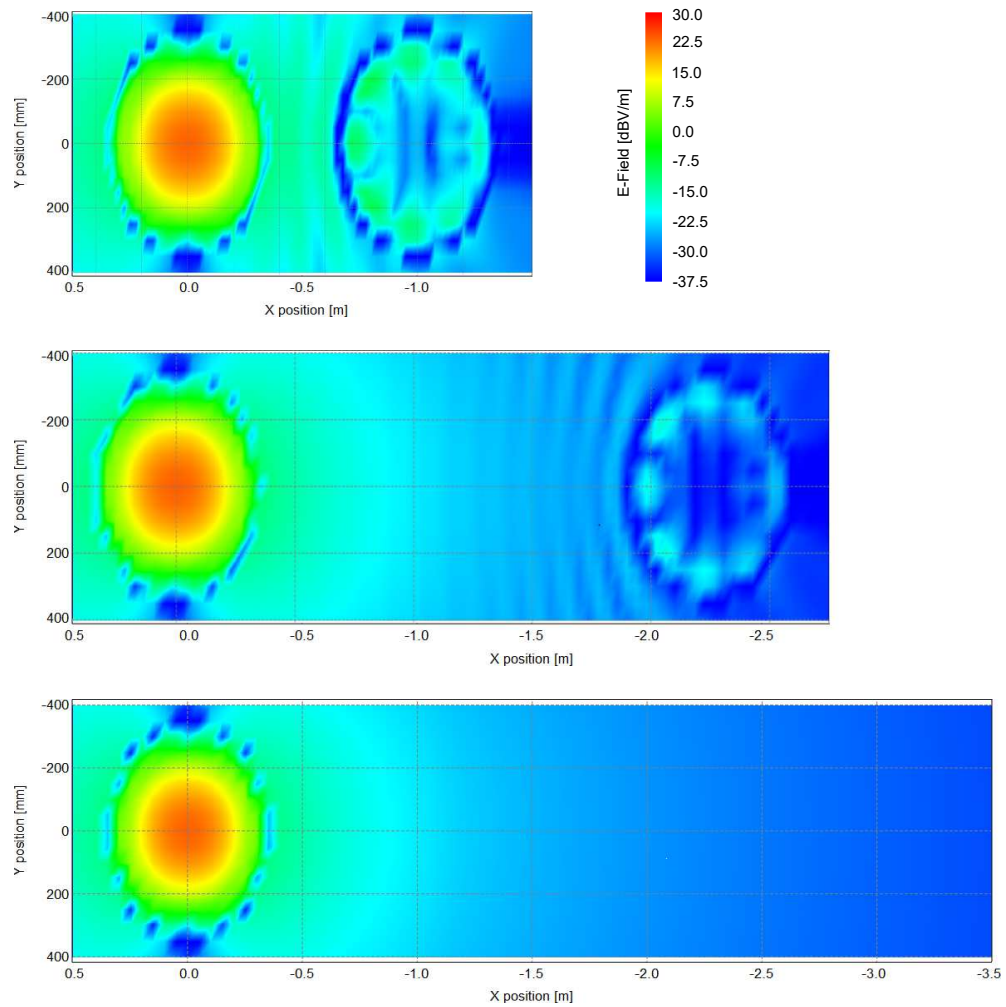


Figure 4-14: Near field at $z = 500$ mm for the single antenna and double antenna setup with a distance of $d_{\text{sweep}} = 1$ m and $d_{\text{sweep}} = 2.25$ m with the color scale representing the electric field strength.. (see text for details)

5 Measurements

5.1 Mechanical Setup

To conduct the measurements with the L-band VeGA antennas, a customised setup had to be built. The following requirements were derived and implemented in the design:

1. Variable distance between the antennas
2. Easy determination of said distance
3. Controlled rotation of one antenna around its z-axis
4. Indicators to easily read off certain rotation values
5. Same height of the antenna flares
6. Option to secure the movable antenna in place
7. Mounting points for the hybrid couplers

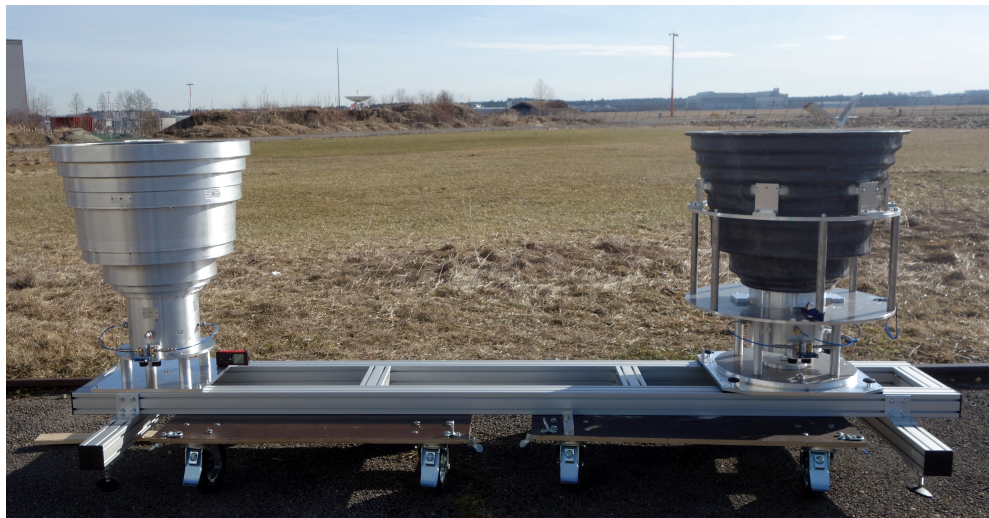


Figure 5-1: Antenna fixture during the assembly for the outside measurement (left: stationary aluminium antenna, right: movable CFK antenna)

These requirements resulted in the setup depicted in figure 5-1, which was built by the mechanical lab of the institute. During previous studies, various versions of the antennas were tested. As explained in section 3.4 the aluminium and the CFK antenna both fulfil the specified performance requirements and are almost identical in their electrical performance.[11] Therefore, both antennas are used in the measurements and treated as equal. It is possible to reuse the mounting structure from the CTR measurement campaign to hold the CFK antenna. Because of the weight advantage of the CFK antenna, the aluminium version is chosen as the stationary antenna. The base frame of the setup is made out of aluminium construction profiles. This enables the fixation of the rectangular base plate of the first antenna while also allowing for a guided movement of the second antenna. The polarization direction can be maintained by fixating

the second antenna with an aluminium pin at 0° .

To repetitively measure the distance between the antennas a laser rangefinder is used. It is mounted on the base plate of the aluminium antenna aiming at a dedicated vertical surface. The distances during the measurements are set taking into account the respective additional distance to the center point of the antennas.

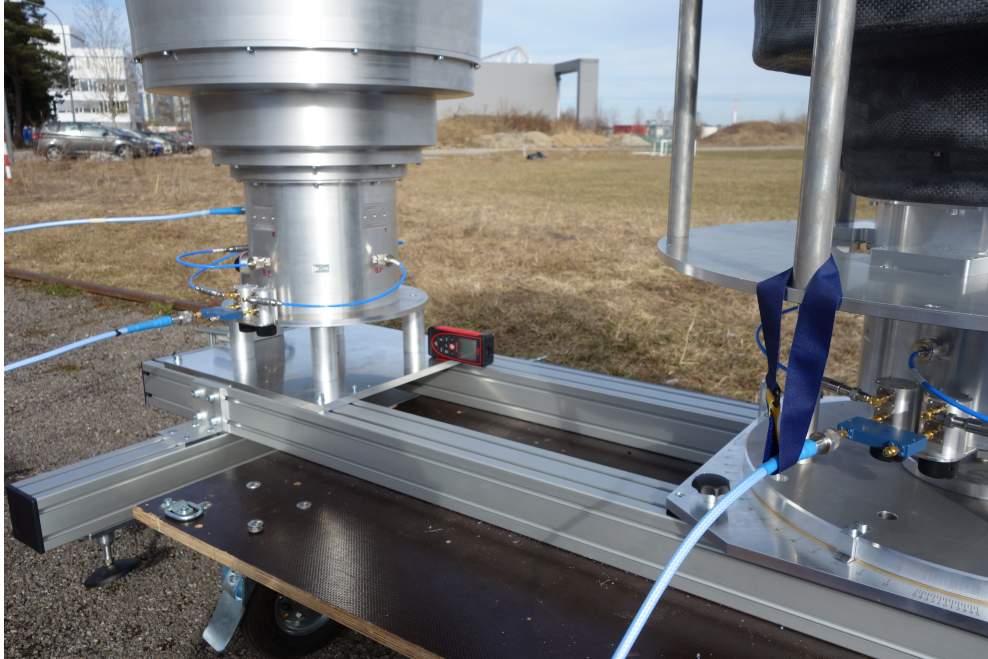


Figure 5-2: Close up image of the measurement setup (visible: hybrid feed networks, laser range finder as well as indicators for the rotation)

The mount of the CFK antenna is placed on a brass plate to facilitate the rotation measurements and to counteract abrasion through friction between the mount and the base plate. Angle indicators are etched into the base plate providing measurement points. For the angular intervals of $0^\circ \pm 5^\circ$ and $90^\circ \pm 5^\circ$ every 0.5° increment is marked. In between, increments of 5° are indicated. Figure 5-2 shows a close up image of the previously described setup.

After both antennas are mounted on the base frame, roller boards are placed under the structure. With these it is possible to securely move the setup outside for the measurements. The measurements are conducted outside to keep the influence of reflections from other structures or buildings to a minimum. The boards remain under the structure to prevent repeated lifting of the setup. The wheels are secured to provide the necessary stability while the second antenna is moved and the measurements are conducted.

5.2 Tuning of the Hybrid Feed Network

To provide the antenna ports with the signals and their respective phase shifts hybrid couplers are utilised. Step attenuators and phase shifters are used during the measurements to omit the intrinsic amplitude and phase imbalance of the hybrid couplers.

The feed networks are tuned to guarantee the same signal amplitude and the 180° phase offset between the two output ports. This is done using a VNA to conduct a 3-port s-parameter measurement.

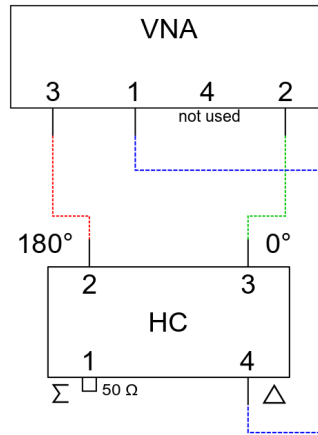


Figure 5-3: Measurement setup for the tuning of the hybrid couplers

The hybrid feed networks are tuned in their final assembly form including the cables which are used later to connect them to the antenna ports. The Rohde & Schwarz ZV-Z52 (model 30) calibration unit is used to calibrate the measurement chain up to the connection point of the hybrid feed network and the VNA. After the calibration, each hybrid feed network is connected to the VNA as shown in figure 5-3.

The magnitudes of S_{21} and S_{31} as well as their phases are displayed on the VNA and markers show the values for $f_0 = 1.2575\text{GHz}$. First, the amplitude is matched using the step attenuators. After that, the phase offset is adjusted. The plot in figure 5-4 shows the magnitude and phase characteristic of the first feed network. Shown in the plot is an excerpt of the VNA measurement. The dashed and dotted line depict the measured values while the third line represents the absolute offset between them. For f_0 the offset is noted in the graph.

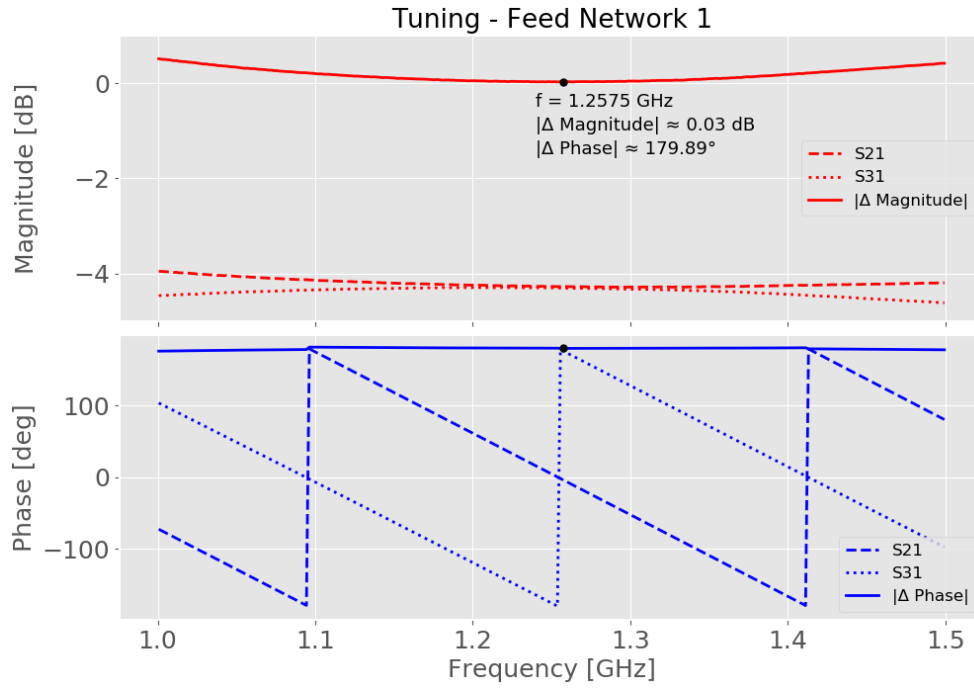


Figure 5-4: Magnitude and phase characteristic of feed network 1 for $f_0 \pm 250$ MHz

The plot shows the behaviour of the feed network for $f_0 = 1.2575$ GHz. The VeGA antenna has a bandwidth of 84 MHz and in this frequency range the magnitude offset can be considered as constant. For the first hybrid feed network the offset between the output ports is approximately 0.04 dB for the lower cut-off frequency $f_l = 1.2155$ GHz as well as the higher cut-off frequency $f_h = 1.2995$ GHz. As explained in the previous chapters, the hybrid coupler equally splits the input signal into two output signals. Therefore, both output channels should show a magnitude of -3 dB in relation to the input port. As can be seen in the plot, both graphs show an attenuation of around 4.4 dB. This can be explained by the insertion loss of the step attenuators [27], phase shifters and cables in addition to possible insertion losses at connecting points. The phase shift is also shown in the plot. For f_l the phase offset between both ports is 180.39° and for f_h the phase offset is 180.07° . Appendix A.2 contains the diagrams of the remaining hybrid feed networks.

5.3 Measurement Setup

The mechanical setup is assembled inside. After the assembly the hybrid feed networks are connected to the antenna ports. The complete setup is then rolled outside on roller boards. The VNA is set up next to the antennas and the measurement chain is calibrated using the calibration unit. After this, the VNA is connected to the feed networks and the measurements are conducted.

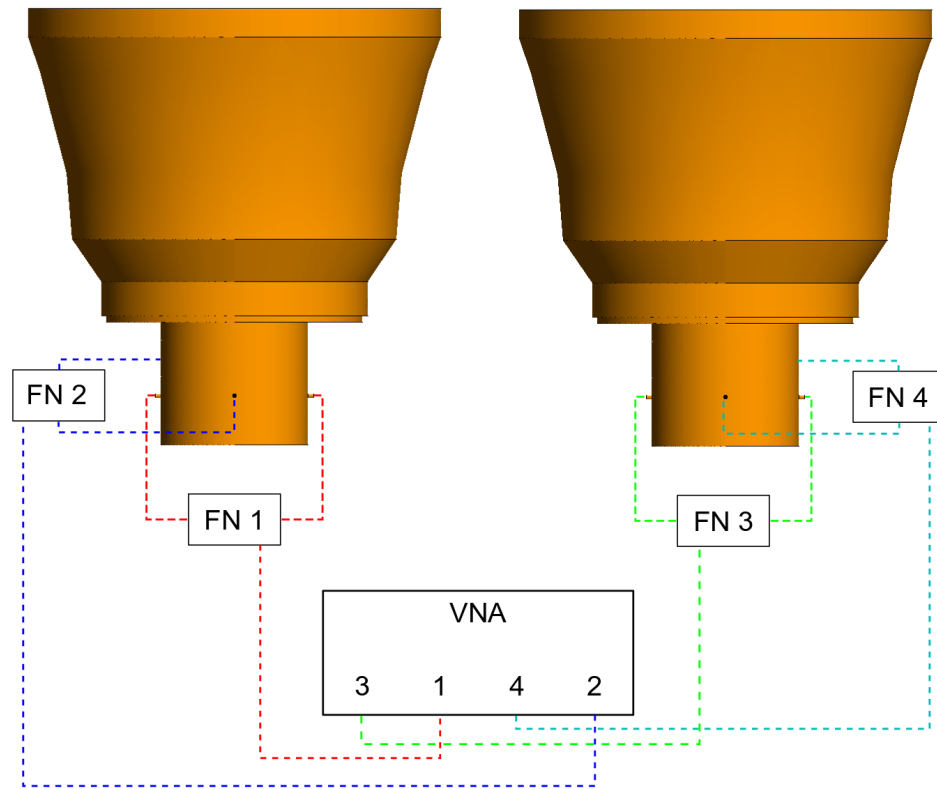


Figure 5-5: Schematic drawing of the measurement setup showing both antennas as well as all feed networks and the VNA

The values for d_{sweep} are chosen in consistence with the simulations. Deviating from the simulation, additional angles were measured. Figure 5-5 shows a schematic view of the measurement setup focussing on the connection of the VNA and the feed networks.

5.4 Measurement Results

In this section the measurement results are discussed. They are also compared to the results of the simulation. In addition to the parameter sweeps, tests with absorbers are conducted to further reduce the antenna coupling.

5.4.1 Normal Antenna Setup

First, the results of the co- and cross-coupling are discussed. After this the inter-channel-coupling and the reflections at the Δ ports of the feed networks are analysed. The results are displayed over the parameter d_{sweep} as well as over the frequency. For each distance five measurements are taken to provide a rough estimate of the statistical uncertainties of the measurement. Their mean value is displayed as a solid line in the graphs while the 2σ uncertainty bounds are shown as semi-transparent areas. The

results of the simulation are included as dashed lines. The systematic uncertainties of the VNA are given in the data sheet as follows. [28](p. 10)

- 0 dB to -55 dB: < 0.1 dB
- -55 dB to -70 dB: < 0.2 dB
- -70 dB to -85 dB: < 1 dB

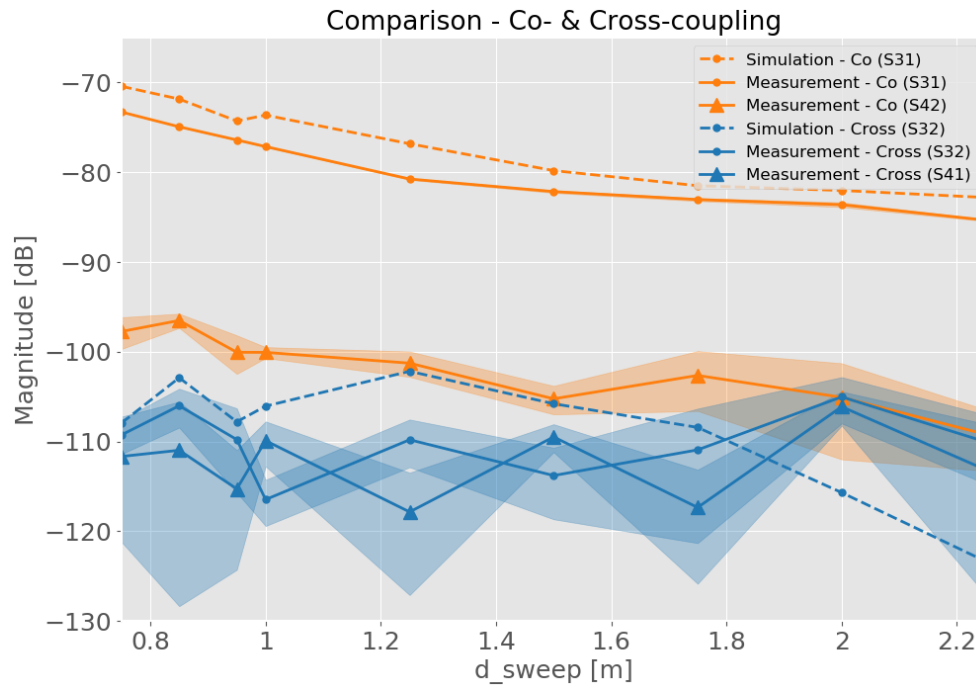


Figure 5-6: Co-coupling for f_0 over d_{sweep}

As the power density decreases with the growing distance between the transmitter and receiver, it is expected that the coupling between the antennas decreases as well. Figure 5-6 shows a comparison between the measurement and simulation for the co- and cross-coupling. For the co-coupling the received polarization on antenna 2 is the same polarization which is transmitted by antenna 1. The cross-coupling reflects the case where the received polarization on antenna 2 is orthogonal to the transmitted polarization of antenna 1.

The graph above shows a maximum difference of -3.9 dB between the measurement and simulation results for S_{31} . The magnitudes decrease with approximately -8 dB m^{-1} in the measurement and with approximately -8.3 dB m^{-1} in the simulation. Compared to the simulated values, it can be noted that the measured values for S_{31} show a good agreement in magnitude and a similar progression.

There is a difference of around 20 dB to 25 dB between the two measured co-coupling parameters. This shows that the antennas influence each other more intensely in a HH

polarization state as they have been specified in chapter 4.1.

The requirement for the co-coupling is set at -90 dB, which, according to these measurements, can only be achieved for S_{31} with a distance greater 2.25m between the antennas or by implementing additional isolation measures. Extrapolating the progression to greater distances suggests that the requirement is met at a distance of around 3 m.

The cross-coupling parameters are also included in the graph above. They are in the range of -100 dB to around -120 dB. Overall, a decrease in magnitude can be seen but the trend is not as pronounced as for the co-coupling. The measured values do not show a clear decreasing trend. As can be seen by the uncertainty bounds, the values fluctuated noticeably during the measurement, which can be attributed to the decreasing accuracy of the VNA for low magnitudes. Nevertheless, it can be noted that the cross-coupling of the antenna lies below -100 dB for f_0 . Overall, the measured progressions verify the simulated values.

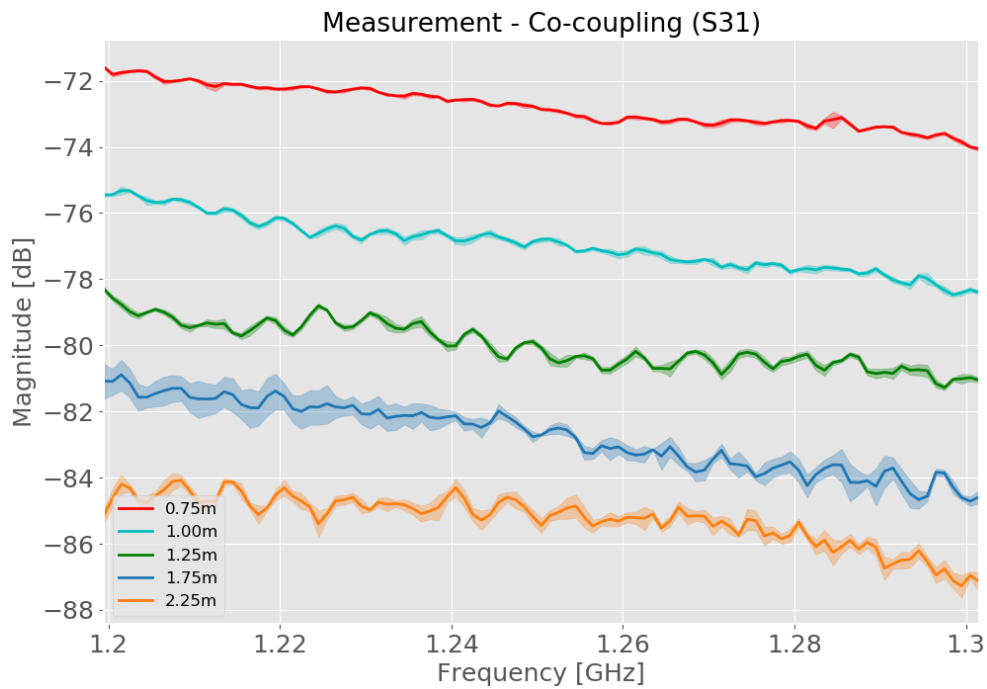


Figure 5-7: Co-coupling coefficient S_{31} over $f_0 \pm 58$ MHz

The graph in figure 5-7 shows the co-coupling parameter S_{31} for $f_0 \pm 58$ MHz. A decrease of the coupling with increasing frequency is observed. It becomes clear, that the previously observed behaviour is not only valid for the center frequency but also for the targeted bandwidth of 84 MHz. The magnitude decreases with the increasing distance.

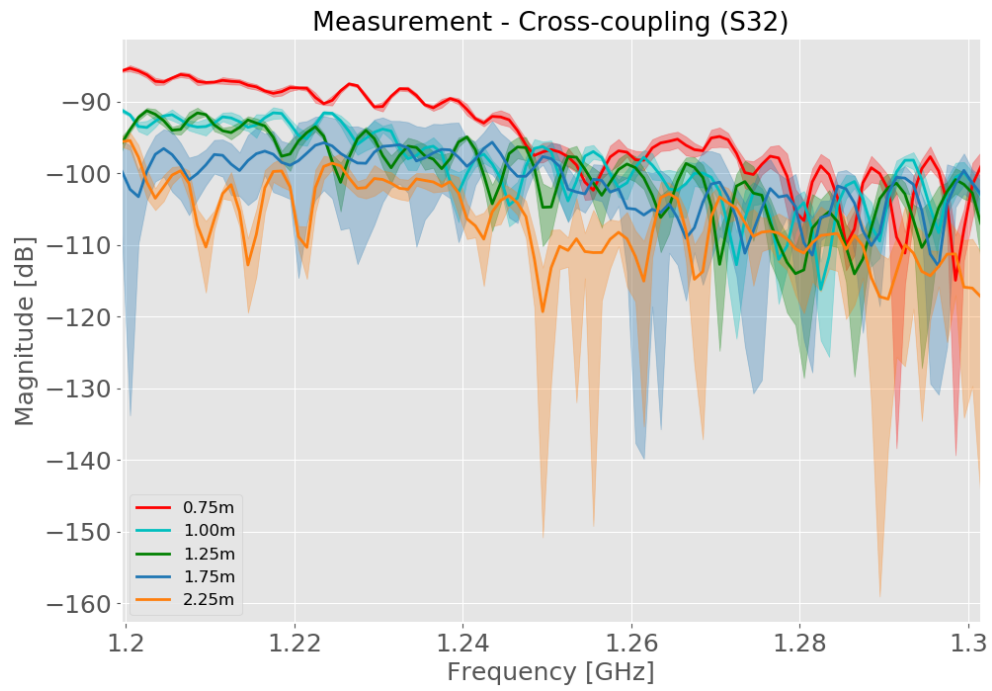


Figure 5-8: Cross-coupling coefficient S_{32} over $f_0 \pm 58$ MHz

Figure 5-8 shows the cross-coupling of the antennas over $f_0 \pm 58$ MHz. Overall, the cross-coupling of the antennas over the relevant frequency range has a maximum magnitudes of around -85 dB for the closest distance (0.75 m).

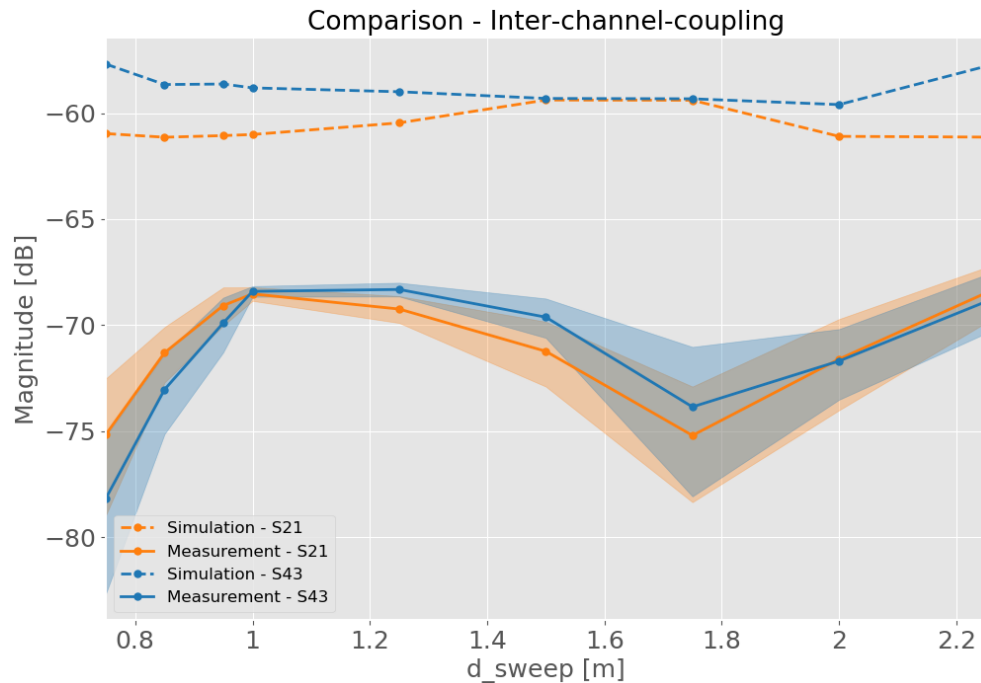


Figure 5-9: Inter-channel-coupling for f_0 over d_{sweep}

The inter-channel-coupling for both antennas is shown in figure 5-9. The parameter S_{21} corresponds to the first antenna, which is made out of aluminium. S_{43} depicts the inter-channel-coupling of the CFK antenna. Both parameters show the same progression and

match within the range of their uncertainties.

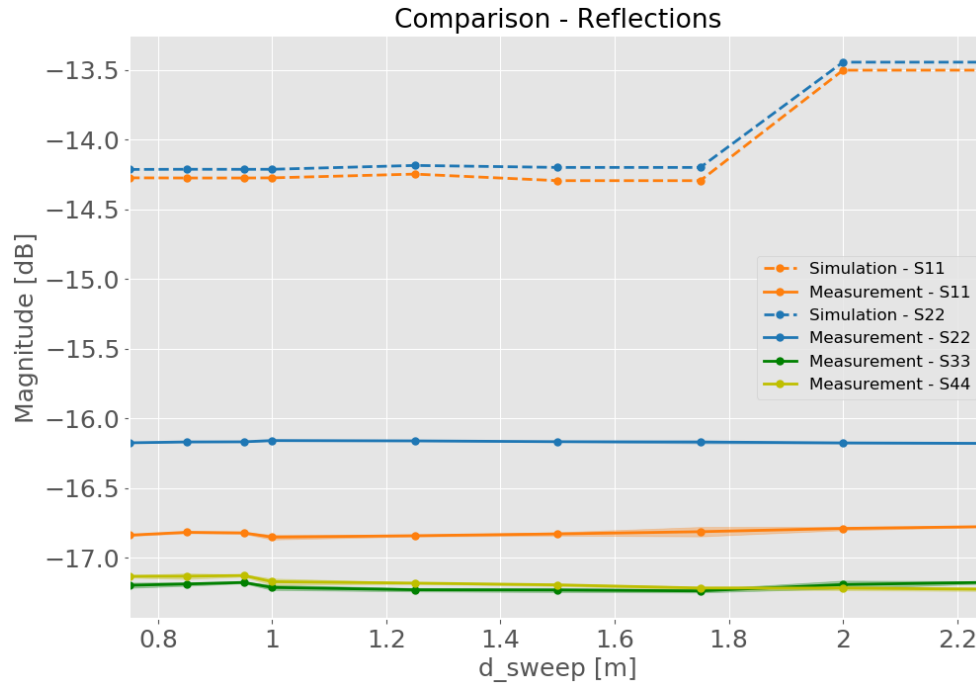


Figure 5-10: Reflections for f_0 over d_sweep

Figure 5-10 shows the input reflection parameters of each feed network. This parameter is in first order to be independent of the distance between the antennas. Therefore, a near constant magnitude is expected for each feed network. Because all networks are made up of the same components, their reflection coefficients should be within the same order of magnitude.

As can be seen in the plot, the graphs are in the same magnitude range and can be considered constant with a maximum deviation of 0.1 dB from their average values. Their magnitudes lie within 1 dB of each other, which is acceptable and could be attributed to slightly different characteristics of the components ... to the feed network.

The measurements for the rotation of the second antenna are conducted in a distance of 1 m between the antennas. Based on figure 2-6 in chapter 2.3, significant changes for the co-coupling were expected starting at 75° and for up to 15° for the cross-coupling. Therefore, intervals of 0.5° were chosen for the first five degrees of the rotation as well as from 85° to 90° . The coupling type given in the diagram, is the type determined for $\alpha_sweep = 0^\circ$.

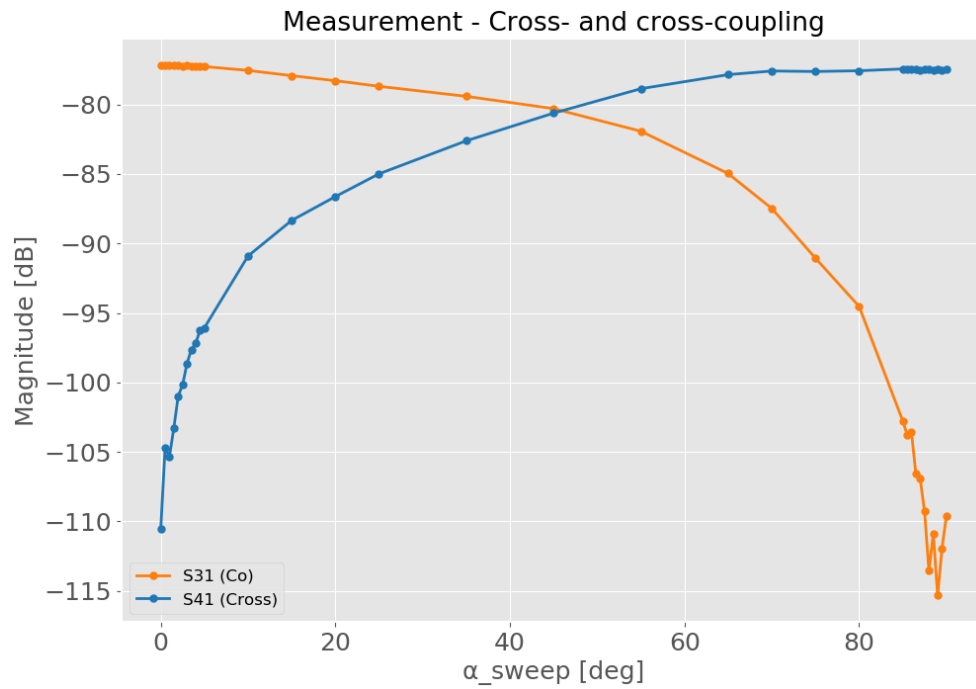


Figure 5-11: Co- and cross-coupling for f_0 over α_{sweep}

Figure 5-11 shows the co- and cross-coupling of the antennas for the rotation of the second antenna. By increasing the rotation to 90° the co-coupling parameters are changed into cross-coupling parameters. Therefore, the co-coupling parameters should decrease in magnitude while the cross-coupling parameters increase.

As expected and shown in chapter 2.3, the values of S_{31} decrease when the antenna is rotated. The values converge towards the values of S_{41} at $\alpha = 0^\circ$. Also, S_{41} converges towards the magnitudes of S_{31} . For a rotation of 45° the magnitudes of S_{31} and S_{41} were expected to be equal, which is in good agreement with the measurements.

The simulated progressions for S_{31} and S_{41} are within the same magnitude and show the same progression for the first 5° (see figure 4-11). The expectations are considered validated through the measurement.

5.4.2 Absorbers

In this section only one of the tested absorber setups is described. Additional tests and their results can be found in appendix A.3. These tests are done on an experimental basis and without measures to ensure the preservation of the antenna gain pattern. Promising options are to be replicated and re-evaluated by analysing the gain pattern with help of the CTR. The setup described here is the fourth measurement setup of the test series. The pyramidal absorbers in these tests are 41.7 cm high with a base of 15.3 cm by 15.3 cm by 4 cm. All measurements are conducted with a fixed distance of 1.25 m between the antennas. Where necessary, tension belts were used for the fixation

of the absorbers.

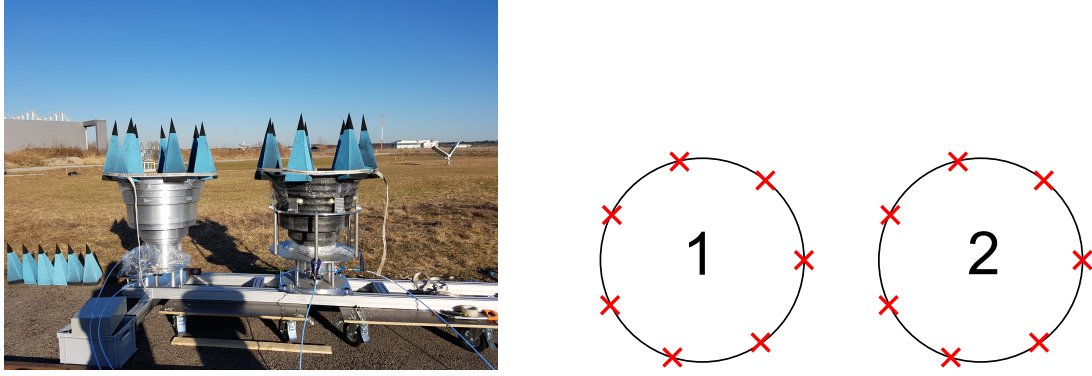


Figure 5-12: Picture of setup 4.3 with an illustration of the corresponding top view, where the absorber placement is marked by red crosses

For this setup seven absorbers are arranged on the top rim of each antenna. They are spaced out evenly. The first measurement is taken when the inner most absorbers of both antennas are facing each other. The absorbers on the first antenna are then moved one step clockwise into the former empty sections. This leaves the absorber on the second antenna facing an empty space. For the last variation the absorbers on both antennas are moved one space clockwise. Now the absorber on the first antenna is facing an empty space on the second antenna. This variation is shown in figure 5-12.

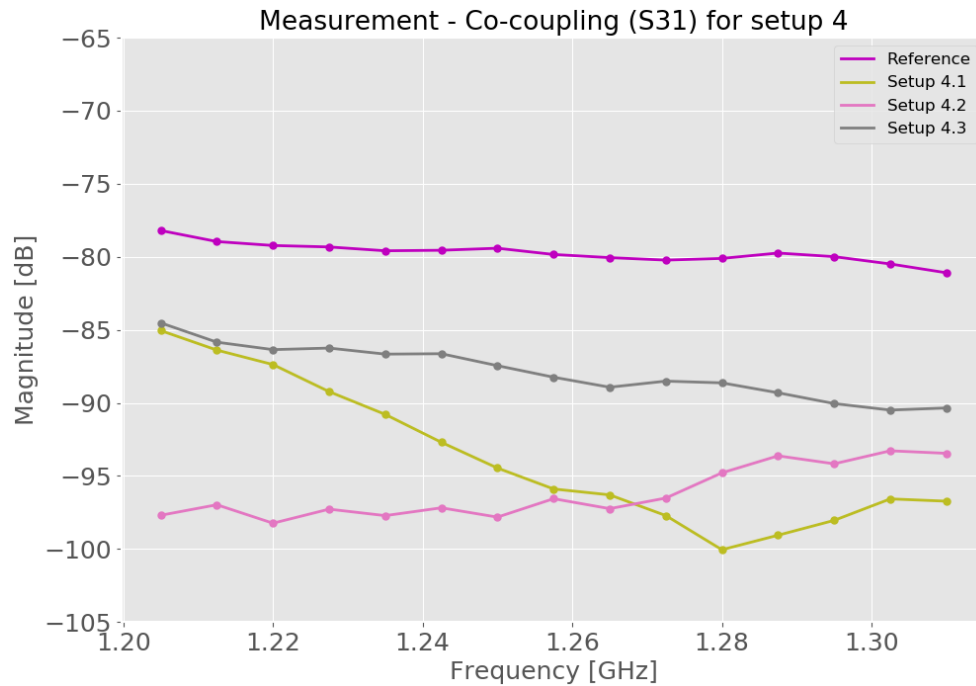


Figure 5-13: Co-coupling coefficient S_{31} over $f_0 \pm 52.5$ MHz of setup 4

Figure 5-13 shows the result of all three variations of the fourth setup. A reference graph is included and represents the antennas at the same distance but without absorbers. For the second variation the co-coupling parameter S_{31} is constantly below

–90 dB. The first variation shows magnitudes below –90 dB for two thirds of the targeted bandwidth of the transponder. Although variation number three, as pictured in figure 5-12, shows an improvement of up to –10 dB, it is not sufficient. A repetition of the measurement in the CTR should be conducted to verify the gain pattern.

6 Conclusion and Outlook

Conclusion

The goal of this thesis was to investigate the mutual coupling effects of VeGA antennas which should be integrated within the new generation of DLR's Kalibri transponders. The antenna coupling has a decisive influence on the transponder design and has therefore to be quantized before first transponder designs can be developed and tested. The decoupling of both antennas in the transponder is required to be at least 90 dB. To investigate the mutual coupling, various simulations were conducted to obtain first reference data. Measurements were executed to provide a definitive statement regarding the dependency of the mutual coupling on the distance and the polarization plane between the antennas. The design of the L-band transponders currently being developed has been adapted based on the results obtained in the course of this thesis.

First, the antenna simulation model was adapted to incorporate feed networks to represent the physical geometry as well as the antenna's feeding system. The simulation model was then expanded further by integrating a second antenna into the setup. To properly characterize the mutual coupling of the antennas, s-parameters were defined as a representative indicators. Parameter sweeps were designed to characterize the complete setup for different distances and various angular mismatches between the polarization planes of the antennas.

The simulations showed a worst case scenario of the antenna decoupling for the s-parameter S_{31} . The simulation showed a continuous decrease of the mutual coupling with increasing distance. For a distance of 0.75 m the coupling is -70 dB and decreases to -86 dB for a distance of 3 m. With the parameter sweep of the angular polarization mismatch the polarization loss factor could be estimated.

In addition, the gain pattern of the antenna was analyzed. In comparison with compact test range (CTR) measurements for a single antenna with feed networks, the simulation model provided matching results. The correct representation of the physical setup in the simulation was therefore verified. Furthermore, the simulated gain pattern remained stable after the integration of the second antenna. For different distances between the antennas, the simulation continuously showed stable results for the co- and cross-polarization gain pattern.

To conduct measurements, a measurement setup was developed and built. In preparation of the measurements, the feed networks were tuned and connected to the antennas. The setup was then installed outside, where the parameter sweeps were conducted.

The results of the distance variation were in good agreement with the simulated magnitudes of the mutual coupling. Between the simulated and measured magnitudes of S_{31} an average difference of approximately 3 dB could be determined. For a distance of 0.75 m the coupling was measured at -73 dB. It decreased to -85 dB for 2.25 m, which was the maximum possible distance in the mechanical setup. Over the relevant frequency range the coupling showed a flat curve with a relatively small decrease in magnitude for each distance. In addition to the results of the distance variation, the measured coupling magnitudes of the angular polarization mismatch agreed with the simulation results.

To further reduce the mutual coupling, absorbers were included in the measurement setup. By utilizing them it was possible to reach the required decoupling of 90 dB at a distance of 1.25 m. Nevertheless, absorbers would drastically increase the overall dimensions of the transponder, might be difficult to attach to the antennas and could need regular replacement due to ageing. Therefore, their use for the new generation of Kalibri transponders is not recommended. Potential solutions are proposed below.

The results of the measurements and simulations are an important input for the design of the transponder. Through them, the distance between the antennas, as one of the main parameters of the transponder design, could be defined. The combination of measurements and simulations has proven to be a suitable method to characterize the mutual coupling of the transponder VeGA antennas in L-band.

Outlook

It is recommended to conduct a CTR measurement campaign to verify the outside measurements. For this, the mechanical setup developed during this thesis can be used. The setup can also be used for further preliminary tests outside.

Absorbers are not a suitable solution to decrease the mutual coupling of the antennas. Furthermore, a calculated distance of approximately 2.9 m between the antennas would be required to ensure the targeted decoupling of 90 dB. In order to reduce this distance, further investigations are necessary. It is already planned to evaluate the use of an aluminium sheet as a bridge between both antennas, which can be modified with cut-outs or ridges to lower the antenna coupling. For the latter, choke ring antennas used for GPS applications can serve as a reference. Depending on the results of according simulations, a test setup can be constructed and tested with the existing mechanical setup.

A vital contribution for the design of DLR's next generation of Kalibri transponders was made by this thesis. The obtained results of the decoupling dependency on the

distance and the mismatch of the polarization angle provide a solid foundation for future investigations.

Bibliography

- [1] Alberto Moreira, Pau Prats-Iraola, Marwan Younis, Gerhard Krieger, Irena Hajnsek, and Konstantinos P. Papathanassiou. A Tutorial on Synthetic Aperture Radar. *IEEE Geoscience and Remote Sensing Magazine*, 1(1):6–43, 2013. doi: 10.1109/MGRS.2013.2248301.
- [2] Sebastian Raab, Daniel Rudolf, Klaus Frank Weidenhaupt, and Marco Schwerdt. Development of DLR’s Innovative Remote Controlled Calibration Targets - Potential of Polarization Sensitive Measurements. In *Proceedings of the European Conference on Synthetic Aperture Radar, EUSAR*. 2014. URL <https://elib.dlr.de/119751/>.
- [3] Microwave and Radar Institute. Internet Page: DLR SAR Calibration Center, . URL https://www.dlr.de/hr/desktopdefault.aspx/tabid-2459/3715_read-53570.
- [4] Constantine A. Balanis. *Antenna Theory: Analysis and Design*. 4 edition, 2016.
- [5] Prof. Dr. Clemen. Script: Elektromagnetische Wellen - Hohlleiter. URL http://www.hs-augsburg.de/~clemen/lehre/Skript_Wellen/8Hohlleiter.PDF.
- [6] H. Henke. *Elektromagnetische Felder: Theorie und Anwendung*. Springer-Lehrbuch. Springer-Verlag, Berlin, Heidelberg, 3., erweiterte aufl. edition, 2007. ISBN 978-3-540-71004-2.
- [7] Klaus Kark. *Antennen und Strahlungsfelder: Elektromagnetische Wellen auf Leitungen, im Freiraum und ihre Abstrahlung*. Springer Fachmedien, Wiesbaden, 5., überarb. u. erw. aufl. edition, 2014. ISBN 978-3-658-03615-7.
- [8] Heinrich Axt. Vergleichende Analyse von Antennenkonzepten für P-Band Kalibriertransponder, 2014. URL <https://elib.dlr.de/90704/>.
- [9] Douglas Bock. Measurements of a scale model ortho-mode transducer, 1999. URL <https://bima.astro.umd.edu/memo/memo74.pdf>.
- [10] Carlos Severino. Compact Feeding System for a P-Band Circular Horn Antenna, 2015. URL <https://elib.dlr.de/95655/>.
- [11] Klaus Frank Weidenhaupt and Marco Schwerdt. CTR Measurement Campaign of L-Band VeGA Antennas. URL <https://elib.dlr.de/122765/>.
- [12] David M. Pozar. *Microwave Engineering*. Wiley, Hoboken, NJ, 4th ed. edition, 2012. ISBN 978-0-470-63155-3.
- [13] Microwave and Radar Institute. Internet Page: Calibration, . URL <https://www.dlr.de/hr/en/desktopdefault.aspx/tabid-2459/>.

- [14] Daniel Rudolf, Björn Döring, Matthias Jirousek, and Marco Schwerdt. A Compact Antenna Rotation Concept for Precise Polarimetric SAR Calibration Transponders. In *Proceedings of the European Conference on Synthetic Aperture Radar, EUSAR*. 2016. URL <https://elib.dlr.de/107810/>.
- [15] Marco Schwerdt, Núria Tous Ramon, Kersten Schmidt, and Patrick Klenk. Overall SAR System Calibration and Validation Plan: Sentinel-1CD, 2017.
- [16] John D. Kraus and Ronald J. Marhefka. *Antennas for all applications*. Tata McGraw-Hill, Delhi, 3rd ed. edition, 2003, 2002. ISBN 0070532435.
- [17] Arthur Ludwig. The Defintion of Cross Polarization. In *IEEE Transactions on Antennas and Propagation*. 1973.
- [18] Sophocles J. Orfanidis. *Electromagnetic Waves and Antennas*. 2016. URL <http://eceweb1.rutgers.edu/~orfanidi/ewa/>.
- [19] Sravan Aitha. Development, Manufacturing and Testing of a P- and L-Band Outdoor Horn Antenna, 2016. URL <https://elib.dlr.de/99283/>.
- [20] Martin Schlup. Script: Wellen auf Leitungen, 2017. URL https://home.zhaw.ch/~hhrt/EL3/7_Leitungen/EL3_Th6_Leitungen.pdf.
- [21] Majid Abbas-Azimi, Farhad Mazlumi, and Fereidoon Behnia. Design of Broad-band Constant-Beamwidth Conical Corrugated-Horn Antennas [Antenna Designer’s Notebook]. *IEEE Antennas and Propagation Magazine*, 51(5):109–114, 2009. ISSN 1045-9243. doi: 10.1109/MAP.2009.5432055.
- [22] R. Gonzalo, J. Teniente, and C. del Rio. Improved radiation pattern performance of Gaussian profiled horn antennas. *IEEE Transactions on Antennas and Propagation*, 50(11):1505–1513, 2002. ISSN 0018-926X. doi: 10.1109/TAP.2002.804002.
- [23] Altair Engineering. *Altair Feko User Manual*. 2018.2 edition, 2018.
- [24] Roger F. Harrington. *Field computation by moment methods*. IEEE Press series on electromagnetic waves. IEEE Press, Piscataway, NJ, 1993. ISBN 9780470544631.
- [25] Altair Engineering. Numerical Methods in Feko: Technical Paper, 2016. URL <https://altairhyperworks.com/product/FEKO>.
- [26] F. Caspers. Rf engineering basic concepts: S-parameters. *CERN Yellow Report CERN-2011-007*, 2011. URL <http://arxiv.org/pdf/1201.2346v1>.
- [27] JFW Industries Inc. Datasheet: Rotary attenuator - Model 50R-254. URL <https://www.jfwindustries.com/pdf/50R-254.pdf>.

- [28] Rohde & Schwarz GmbH & Co. KG. Datasheet: R&S ZVA - Vector Network Analyzer, 2014. URL https://scdn.rohde-schwarz.com/ur/pws/dl_downloads/dl_common_library/dl_brochures_and_datasheets/pdf_1/ZVA_dat-sw_en_5213-5680-22_v1100.pdf.

A Appendix

A.1 Antenna Model

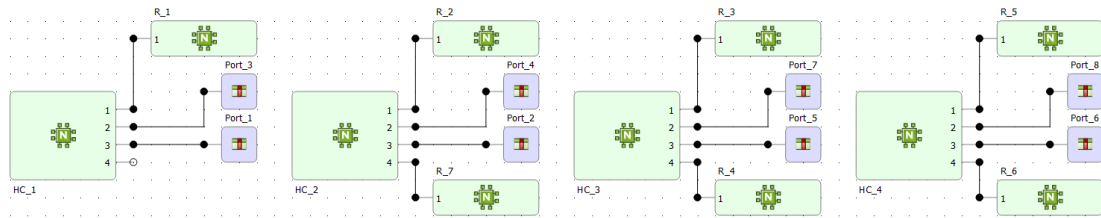


Figure A.1-1: Networks of the model in the schematic view for the calculation of the field patterns with horizontal polarisation of the first antenna. Not visible in this view are the voltage sources connected to the terminals HC1.4

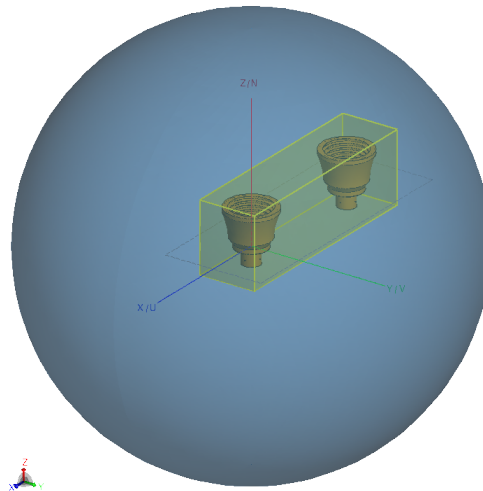
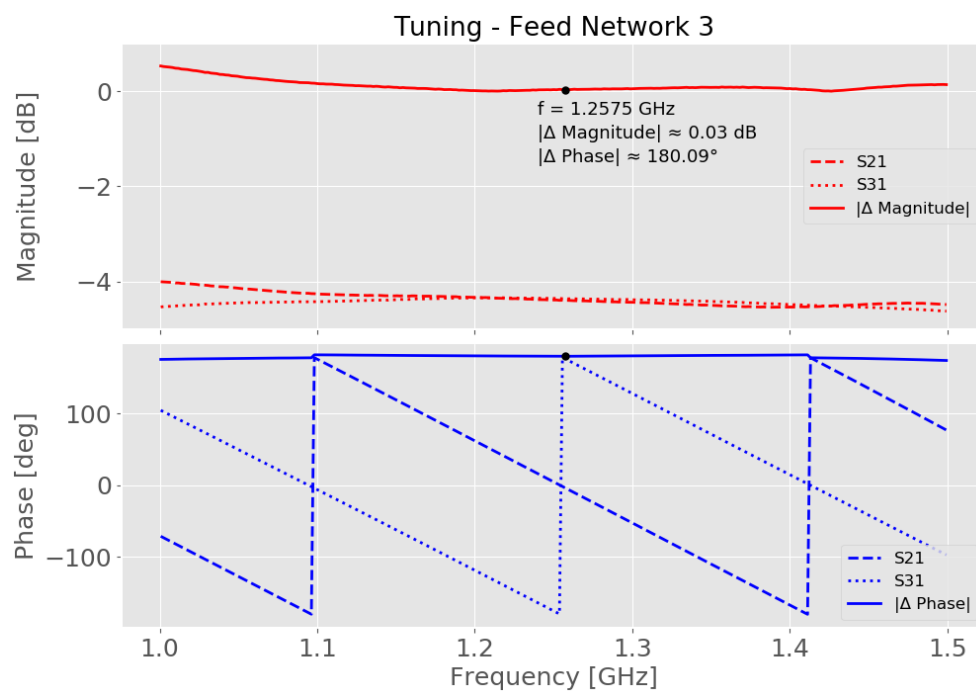
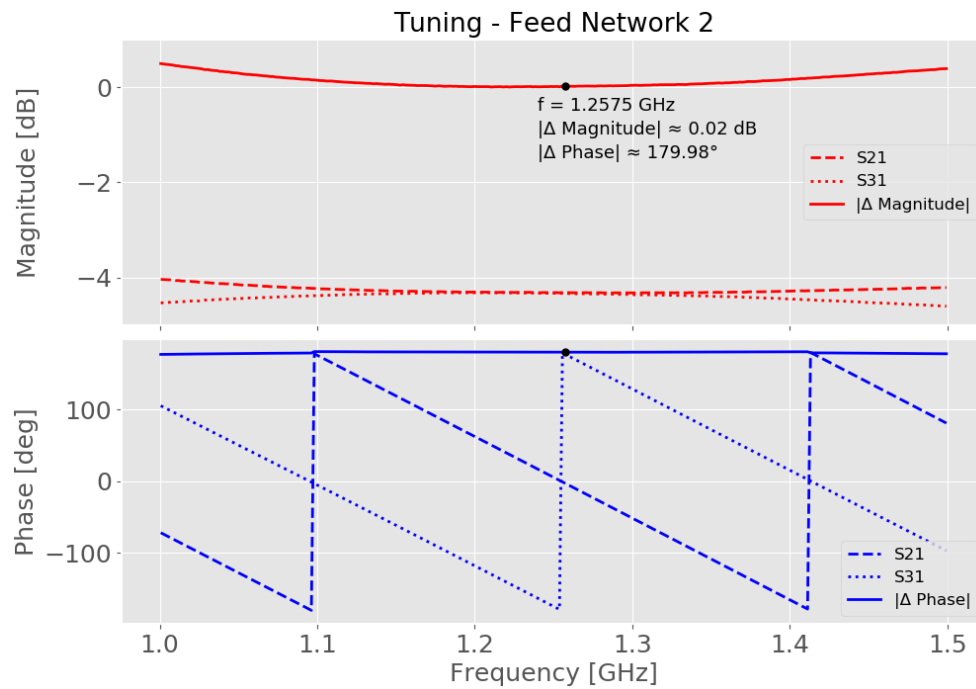


Figure A.1-2: Representation of the requested fields for the antenna model

A.2 Hybrid Feed Networks



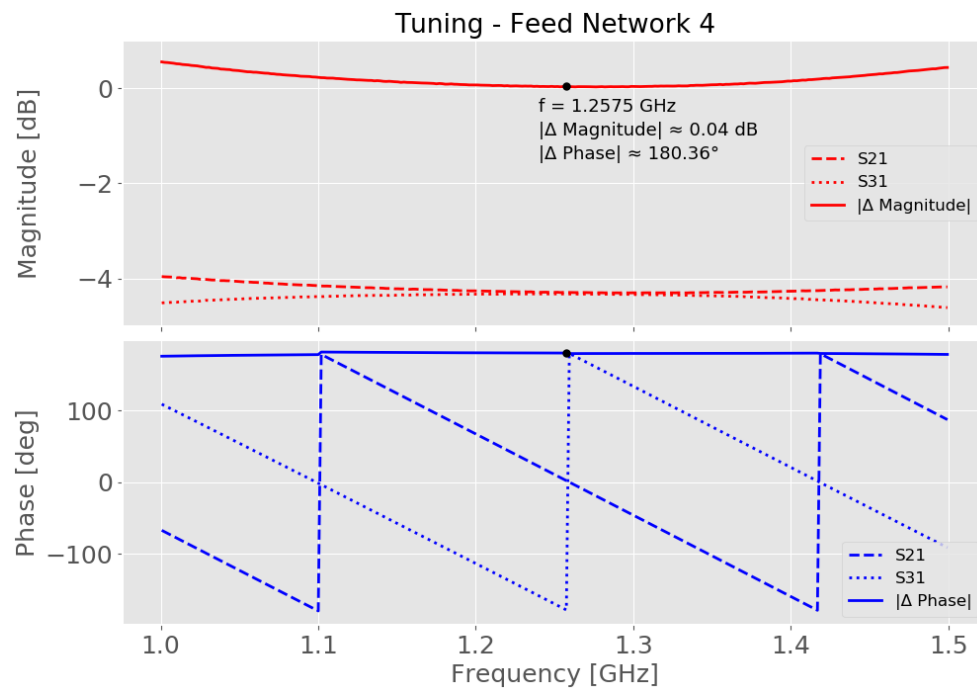


Figure A.2-3: Magnitude and phase characteristics of all hybrid feed networks

A.3 Absorber Measurements

In addition to the tests described in chapter 5, various other tests were done in the same distance of 1.25 m.

For the first setup absorber plates are used. Two plates, of which 13 cm protrude over the antenna rim, are attached to each antenna. They are held in place by tension belts. The setup is shown in figure A.3-4.

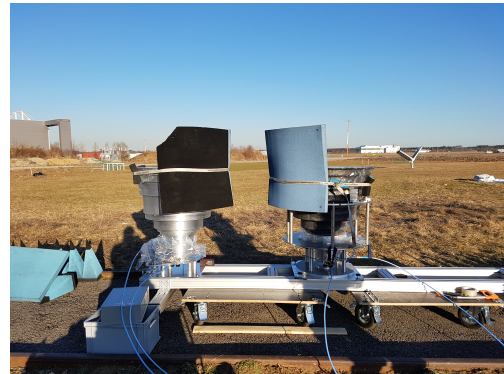


Figure A.3-4: Setup 1

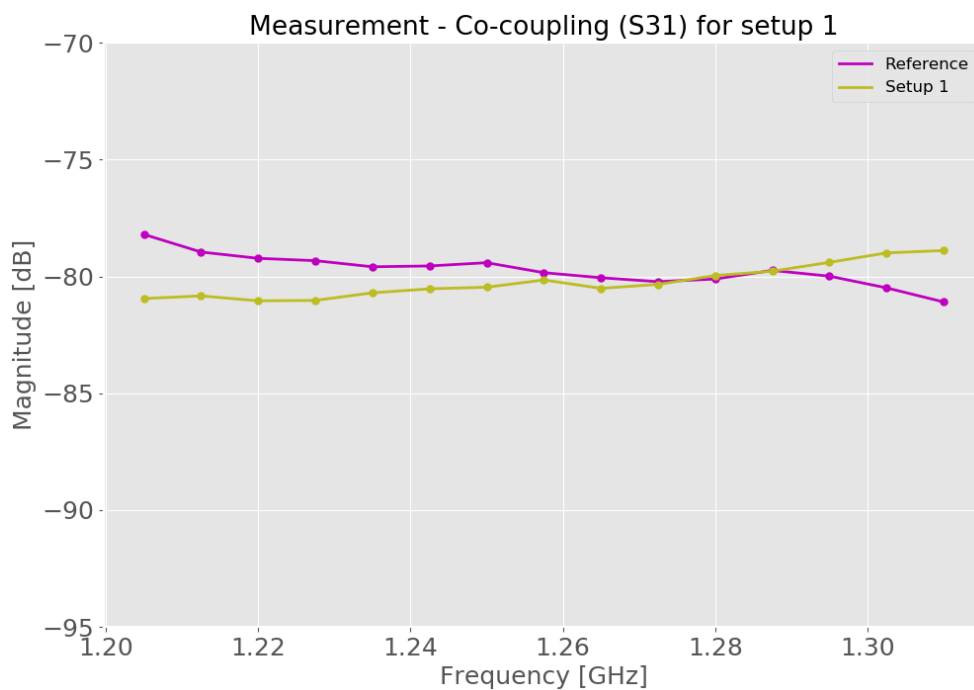


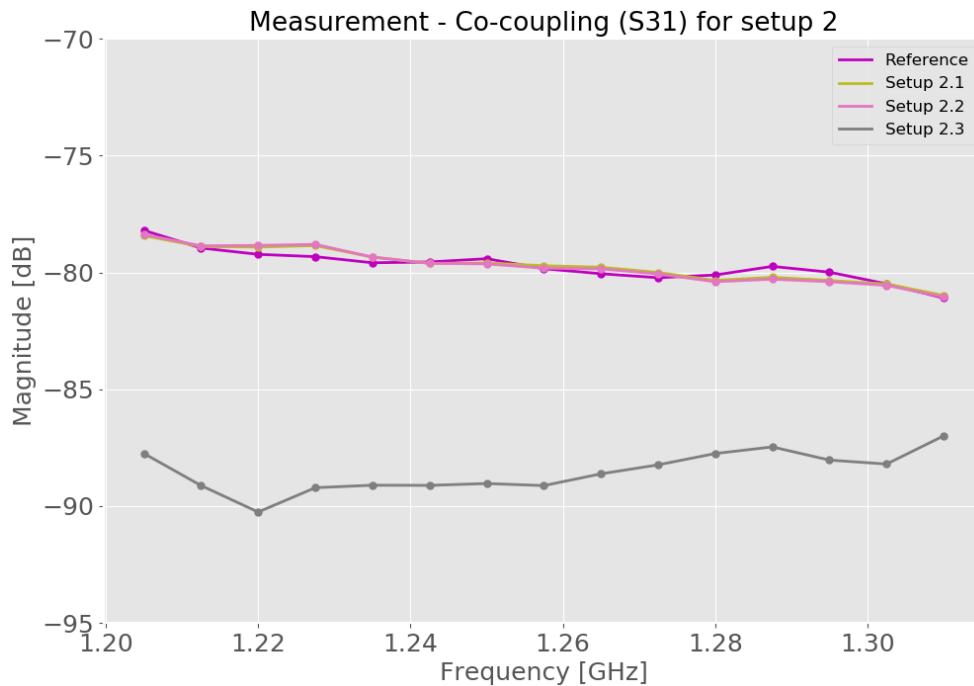
Figure A.3-5: Co-coupling coefficient S_{31} over $f_0 \pm 52.5$ MHz of setup 1

Figure A.3-5 shows the co-coupling coefficient S_{31} over the frequency. In this and all future plots regarding the absorber measurements a reference graph is included. The reference was measured for the same distance between the antennas but without any absorbers. As can be seen in the plot the absorber plates did not improve the co-coupling between the antennas.

Starting with the second setup pyramid absorbers are used. Three different variations of the setup are measured. The first variation consists of absorbers strapped horizontally between the antennas. In the second variation additional pyramid absorbers are placed on the rails between both antennas. For the last version the absorbers on the rails are removed and a row of single absorbers is placed on top of the strapped on absorbers. This setup is depicted in figure A.3-6.



Figure A.3-6: Setup 2.3

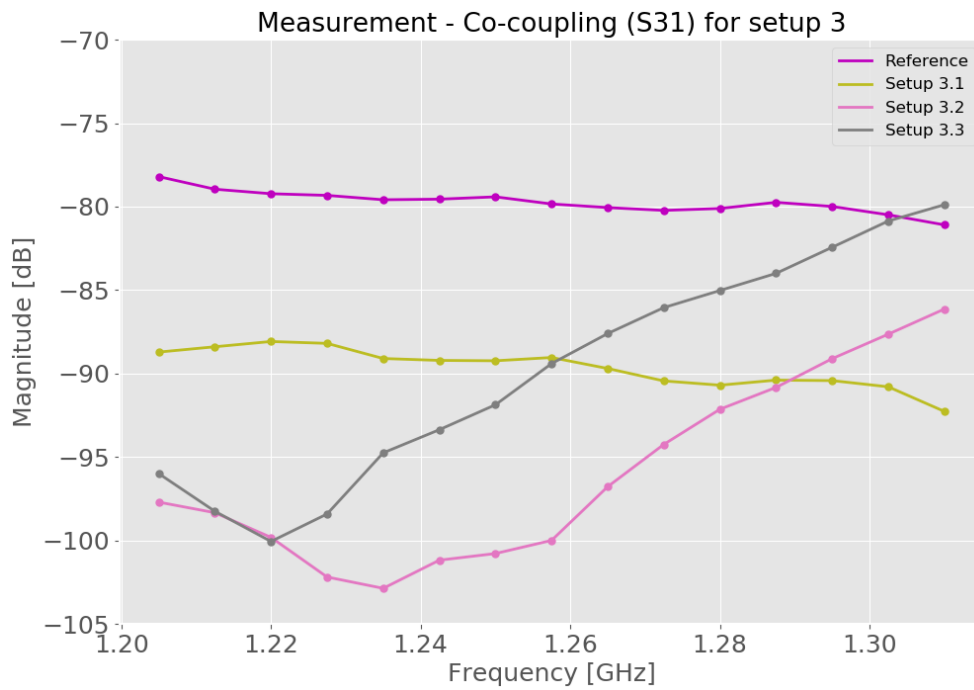
Figure A.3-7: Co-coupling coefficient S_{31} over $f_0 \pm 52.5$ MHz of setup 2

The plot in figure A.3-7 shows no improvement and the same progression for the first and second variation of the setup. An average improvement of -8.8 dB is made with the third absorber setup. As absorbers are placed close to the aperture of the first antenna, they might influence the gain pattern. This setup has to be measured inside the CTR to verify a correct antenna pattern.

For the third setup the absorbers are placed on top of the rim of the antennas. The first antenna is fitted with absorbers touching each other for the first variation. For the second version the same is done for the second antenna. Lastly, every second absorber on the first antenna is removed. This leaves seven absorbers on the first antenna. This variation is shown in figure A.3-8.



Figure A.3-8: Setup 3.3

Figure A.3-9: Co-coupling coefficient S_{31} over $f_0 \pm 52.5$ MHz of setup 3

The results for the co-coupling coefficient S_{31} of the third setup are shown in figure A.3-9. While the second and third version of the setup show an improvement of around -15 dB for the lower frequency half, the measured magnitudes increase constantly. Therefore, these versions are not suitable to further reduce the co-coupling. In contrast to this, the first version of this setup lowers the co-coupling an average of -9.9 dB. This makes setup 3.1 a viable option, which should be tested in the CTR.

For the last setup small offcuts of absorbers are used. They are placed on both antenna rims with equal distances to each other. On the first antenna additional offcuts are placed on the part which is facing the second antenna.



Figure A.3-10: Setup 5

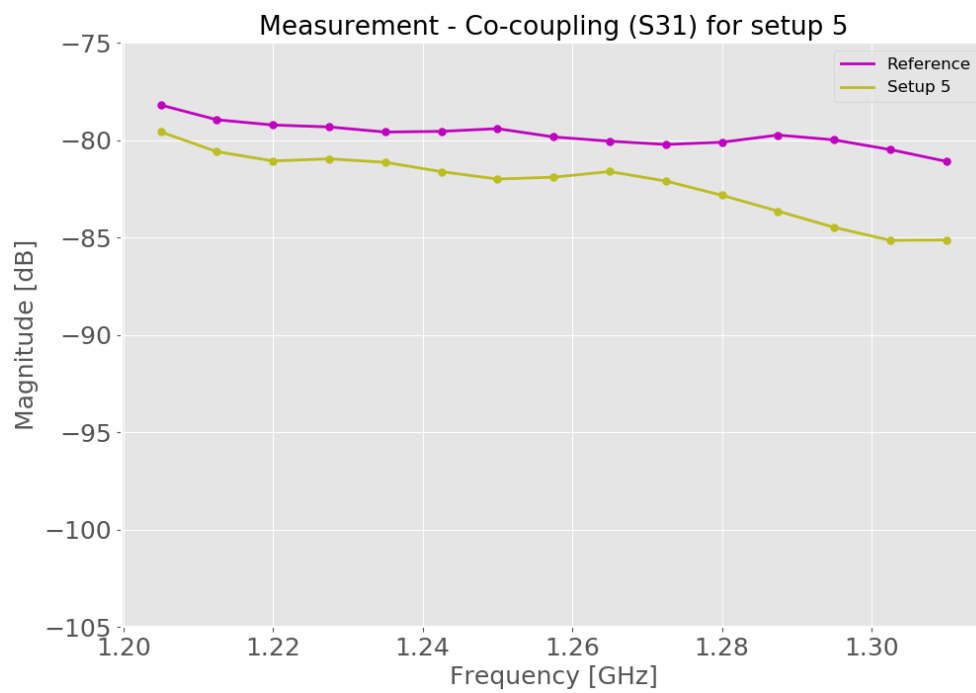


Figure A.3-11: Co-coupling coefficient S_{31} over $f_0 \pm 52.5$ MHz of setup 5

The graph shows only minor improvement when using the absorber offcuts like this. Therefore, this also is not a viable option for the transponder design.

A.4 German Translation of Important Terms

Antenna	Antenne
Antenna efficiency	Antennenwirkungsgrad
Bandwidth	Bandbreite
Co-polarization	Copolarisation
Cross-polarization	Kreuzpolarisation
Corrugated horn	Rillenhorn
Directivity	Richtfaktor
Far field	Fernfeld
Gain	Gewinn
Main lobe	Hauptkeule
Receiver	Empfänger
Reflection coefficient	Reflexionsfaktor
Side lobe	Nebenkeule
Transmission line	Übertragungsleitung
Transmitter	Sender
Waveguide	Hohlleiter

Theses

1. Compared to previous measurements, a complex simulation model of an antenna including its feed system can produce almost identical results.
2. Preliminary results regarding the mutual coupling of two VeGA antennas can be achieved through simulations with different parameter sweeps.
3. A measurement setup can be designed and built on the basis of preliminary simulation results.
4. The expected behaviour of the mutual coupling can be verified through measurements using a suitable measurement setup.
5. The implementation of additional structures like absorbers can reduce the mutual coupling between the antennas.
6. By combining simulations and measurements, reliable and quantitative predictions of the mutual coupling between two VeGA antennas can be made.
7. A recommendation on how to achieve an antenna decoupling of 90 dB can be made and provide an important basis for the overall design of a calibration transponder.

Statement of Authorship

I hereby declare that the thesis submitted is my own unaided work. All direct or indirect sources used are acknowledged as references. This paper was not previously presented to another examination board and has not been published.

Place, Date

Signature